Research Square

Preprints are preliminary reports that have not undergone peer review.
They should not be considered conclusive, used to inform clinical practice,
or referenced by the media as validated information.

CCL24+ dermis-resident macrophages sustain Leishmania major persistence after clinical healing within a spatially segregated, type 2 immune niche

David Sacks

dsacks@niaid.nih.gov

NIAID

Sang Hun Lee

NIH https://orcid.org/0000-0002-5167-0077

Tiago Ferreira

FMRP-USP https://orcid.org/0000-0003-4894-1515

Byunghyun Kang

NIH

Olena Kamenyeva

National Institutes of Health https://orcid.org/0000-0002-6541-5616

Margery Smelkinson

NIH

Article

Keywords:

Posted Date: November 4th, 2026

DOI: https://doi.org/10.21203/rs.3.rs-11245215/v1

License: This work is licensed under a Creative Commons Attribution 4.0 International License.
Read Full License

Additional Declarations: There is **NO** Competing Interest.

Title: CCL24^{+} dermis-resident macrophages sustain *Leishmania major* persistence after clinical healing within a spatially segregated, type 2 immune niche

Authors: Sang Hun Lee[1]*, Tiago Rodrigues Ferreira[1], Byunghyun Kang[2], Olena Kamenyeva[3], Margery Smelkinson[3], and David L. Sacks[1]*

Affiliations:

[1]Laboratory of Parasitic Diseases and [2]Laboratory of Molecular Immunology National Institute of Allergy and Infectious Diseases, National Institutes of Health, Bethesda, MD 20892, USA.

[3]Biological Imaging Section, Research Technology Branch, National Institute of Allergy and Infectious Diseases, National Institutes of Health, Bethesda, MD 20892, USA.

* Correspondence should be addressed to S.L (leesh2@nih.gov) and D.L.S. (dsacks@niaid.nih.gov)

Abstract

Persistent infection following clinical cure is a hallmark of *Leishmania* infections. It remains poorly understood despite its importance for disease reactivation and parasite transmission. Here, we identify CCL24^{+} dermal tissue-resident macrophages (TRMs) as the principal host cells harboring *L. major* in healed ear lesions of C57BL/6 mice. Histologic examination and multiplexed imaging of healed dermal lesions revealed that the infected cells were found within small, focalized areas of inflammation distinguished by the presence of infiltrating iNOS^{+} inflammatory monocytes, eosinophils and T cells, with high intracellular parasite loads confined to the dermal TRMs. Spatial transcriptomic analyses of healed skin confirmed the presence of small inflammatory foci characterized by monocytes, neutrophils, CD4^{+} and CD8α^{+} T cells, and strong enrichment of IFNγ-responsive genes. Embedded within this type 1 inflammatory environment, the strongest parasite signals were localized to spatially segregated dermal niches that were enriched for type 2 associated transcripts, including *Il4*, *Arg1*, *Retnla,* and TRM-derived *Ccl24* and *Tslp*. Mice with conditional deficiencies that compromised the number and M2-like activation state of the dermal TRMs, including IL-4/13-produced by eosinophils, TSLP produced by the TRMs, and IL-5-producing ILC2s, led to more efficient clearance of residual parasites, including their complete elimination from the site. Post-healing treatments, including IL-5 neutralization, or direct ablation of dermal TRMs in *Ccl24-Cre:DTR* mice, reduced persistent parasite burdens, in some cases to undetectable levels. Together, these findings provide direct spatial evidence that persistent pathogens can survive within localized immune-refractory tissue niches despite otherwise effective host immunity, and identify the regulatory cells and cytokines that can be targeted to achieve sterile cure.

Introduction

Similar to other infectious diseases such as tuberculosis, toxoplasmosis, and herpes virus infections, a hallmark of leishmanial diseases is that they are caused by pathogens that produce persistent infections. In human leishmaniasis, persisting infection following clinical healing is confirmed by detection of low numbers of organisms in lymphoid tissue and/or at the site of the former skin lesion [1, 2, 3, 4]. Such latent infections can lead to reactivation pathologies at the primary or distal site of infection. Reactivation diseases that can occur following self-healing or successful chemotherapy include post-kala-azar dermal leishmaniasis (PKDL), recrudescence of localized cutaneous lesions (recidivans type), and development of mucocutaneous lesions months or years after healing of a cutaneous ulcer (espundia) [5, 6, 7, 8, 9]. Low numbers of persisting organisms in the skin can also establish the hosts as long-term transmission reservoirs, as demonstrated using animals with healed infections exposed to the bites of vector sandflies [10, 11, 12].

The mechanisms underlying the persistence of residual parasites following clinical healing have been studied in mouse models of self-healing cutaneous leishmaniasis. A favored model involves C57BL/6 (B/6) mice infected in the footpad or ear dermis with *L. major*, which for most *L. major* strains will result in a small nodular lesion that spontaneously heals after a few weeks or months, but will fail to completely eliminate the infection [13, 14]. In this classical T_H1 model of acquired resistance, the immune mechanisms responsible for maintaining clinical healing are well described, with inhibition of $CD4^+$ or $CD8\alpha^+$ T cells, IL-12, INFγ, or iNOS during the healed state sufficient in each case to reactivate the development of lesions [15, 16, 17]. The healed mice also maintain a strong and durable resistance to secondary challenge, referred to as concomitant immunity, meaning that the protection against reinfection coincides with the persistence of the primary infection [18]. The inability of this immunity to achieve a sterile cure is poorly understood. Fibroblasts and adipocytes - cells with limited antimicrobial capacity - have been proposed as potential reservoirs [19, 20]. Other non-canonical host cells, including mast cells,

eosinophils, lymphocytes, epithelial cells, mesenchymal stem cells, myocytes, endothelial cells, and keratinocytes, have also been suggested [21]. However, none of these cell types have been definitively shown to harbor persistent parasites in the skin after healing of cutaneous lesions.

Our prior studies have drawn attention to the heterogeneity of myeloid populations found in the ear dermis of B/6 mice infected with a non-healing strain of *L. major* [22]. We showed that the non-healing phenotype was critically dependent on a population of embryonic derived tissue-resident macrophages (TRMs) in the dermis that was preferentially infected in comparison to the macrophage and dendritic cell populations of hematopoietic origin. The outstanding feature of the dermal TRMs was their ability to retain an M2-like phenotype within the strong T_H1 immune environment of the *L. major*-infected skin. The dermal TRMs were found to contribute to their own maintenance by producing CCL24 (eotaxin2) and thymic stromal lymphopoietin (TSLP), which functioned to establish localized type 2 circuitries involving the TRMs, eosinophils, and ILC2s [23, 24].

In the current studies, we investigate the heterogeneity of dermal cells that remain infected following complete resolution of lesions produced by a healing strain of *L. major*. Using multiplex imaging and spatial transcriptomics, we report that the dermal TRMs are the predominant infected cells found in the skin after clinical healing. The infected cells are localized within a type 2 microenvironment whose constituent cells and cytokines can be therapeutically targeted to promote sterile cure.

Results

Dermal TRMs are the predominant infected cells after clinical healing

We confirmed that the *Leishmania major* Friedlin (LmFn) strain produces a non-ulcerative, nodular lesion in C57BL/6 (B/6) mice which eventually heals following a low dose infection of 1,000 metacyclic promastigotes in the ear dermis (Fig. 1A and sFig. 1A). Seventy-

two percent (26/36) of the ears from infected B/6 animals achieved clinical healing by 24 weeks post-infection, characterized by the absence of skin induration or erythema at the inoculation site (sFig. 1B). Despite the absence of overt clinical pathology, all healed ears contained detectable parasites, averaging 400 viable parasites as determined by limiting dilution of whole ear tissue homogenates (Fig. 1B). Dermal TRMs ($CD206^{hi}$ $Ly6C^{int}$) were identified as the predominant phagocytes harboring parasites at 24 weeks post-infection (Fig. 1C). Other sorted myeloid populations, including $Ly6C^{hi}$ inflammatory monocytes and $Ly6C^{low\ to\ int}$ monocyte-derived cells (moDCs), each contained infected cells but harbored relatively fewer viable parasites.

To determine the anatomical distribution of persisting parasites in clinically healed ears, we performed whole-mount imaging of the inner ear skin, where parasites were originally inoculated, enabling high-resolution, three-dimensional visualization of the dermal immune landscape [25]. Examination of multiple ears at 24 weeks post-infection revealed localized parasites within small, spatially segregated foci composed of only a few infected cells and associated with infiltration of both $SiglecF^{+}$ eosinophils and T cells (Fig. 1F). By contrast, ear tissue from mice at 12 weeks post-infection, during the regression phase of disease, exhibited features characteristic of active infection, including larger clusters of infected cells and inflammatory leukocytes aggregated near the presumed site of parasite inoculation (Fig 1E).

To comprehensively evaluate the diversity of cellular phenotypes and their activation states at sites of persistent infection, we performed multiplexed imaging using the Iterative Bleaching Extends Multiplexity (IBEX) technique, which is not readily adaptable to whole-mounted ear tissue [26]. Because persistent infection occurs in the absence of overt pathology and infected foci are sparse, we increased the likelihood of detecting parasite-containing sites within 8-μm tissue sections by generating vertical sections from two ear stacks, each comprising 12 clinically healed ears (Fig. 2A). Detailed examination of H&E-stained vertical sections revealed focalized areas of immune infiltration within the dermis and hypodermis in a subset of

ear slices (Fig. 2B, lower slice, insets 1 and 2). These regions contained cells harboring multiple intracellular amastigotes. Notably, the lower ear slice maintained the overall structural integrity of the skin despite the presence of infected cells and focal inflammation. Intracellular amastigotes, MR^+ dermal TRMs, $iNOS^+$ cells, $SiglecF^+$ eosinophils, neutrophilic granules containing myeloperoxidase (MPO), and $CD4^+$ and $CD8\alpha^+$ T cells were readily observed within the inflamed region (Fig. 2C). Heavily parasitized cells were predominantly confined to MR^+iNOS^- dermal TRMs (Fig. 2C, insets 1 to 4, left panel). The inflamed regions also contained substantial numbers of $MR^-CD11b^+F4/80^+$ cells (Fig. 2C, insets 8 and 9, middle panel), previously identified moDCs [22]. A large fraction of these cells expressed iNOS, with some containing only a single or low number of parasites (Fig. 2C, insets 5 and 6, left panel). In addition, some T cells were observed actively producing IFNγ (Fig. 2C, insets 11–14, right panel).

Spatial transcriptomics reveals parasite persistence within a dermal TRM-associated niche

To further define the cellular composition and immune microenvironment associated with persistent LmFn infection, we performed high-resolution spatial transcriptomic analysis using the Xenium platform (10x Genomics) [27] on four vertically stacked ear sections derived from two paraffin blocks (two sections per block), designated Region_1 - 4. A custom Xenium panel comprising 742 mouse genes and 10 LmFn genes was designed to identify host cell populations, parasite transcripts, and local immune signatures associated with parasite persistence. For cell segmentation, nuclei were first identified from Xenium morphology DAPI images using the StarDist 2D Versatile Fluorescence model. These nuclear masks were then used as priors for transcript-based cell segmentation with Baysor (v0.7.1; scale = 12, min-molecules-per-cell = 30, prior segmentation confidence = 0.7). After quality-control filtering, cells from all four regions were integrated for downstream analyses.

Unsupervised clustering identified 12 major cell populations consisting of both non-hematopoietic and immune cell types (sFig. 2A and B). As expected, because the majority of the healed ear tissue remained in a steady-state condition, the cellular landscape was dominated by non-hematopoietic populations. Among the immune populations, resident skin cells, including dermal TRMs, mast cells, Langerhans cells, and epidermal γδT cells, comprised the predominant leukocyte populations. Inflammatory monocytes represented the principal infiltrating population detected across the tissue sections and exhibited strong expression of IFNγ-inducible genes, including *Cxcl9* and *Cxcl10* (sFig. 2B). Thus, we used *Cxcl9* expression to visualize the inflammatory foci where we expected persistent parasites to be found. Spatial mapping revealed discrete regions of elevated *Cxcl9* expression throughout the stacked ear slices (Fig. 3A and sFig. 3C). Based on these patterns, inflamed ROIs were selected from areas exhibiting focal *Cxcl9* expression, whereas matched non-inflamed ROIs were selected from adjacent areas of the same ear slice with minimal *Cxcl9* expression. To determine whether these inflammatory regions corresponded to sites of parasite persistence, we examined the spatial distribution of parasite transcripts. Although parasite transcripts were sparsely detected, weighted parasite-density analysis, which integrates local parasite transcript detection and clustering, identified discrete parasite-rich microfoci within Cxcl9-positive inflammatory ROIs. The most prominent microfoci were observed in R1_infl_1 (Region1_inflamed ROI_1), R2_infl_2, R2_infl_4, R3_infl_4, R4_infl_1, and R4_infl_5. The limited recovery of parasite transcripts likely reflects the substantially lower abundance of *Leishmania*-derived RNA relative to host transcripts.

Subsequent analyses were restricted to cells located within inflamed ROIs and adjacent non-inflamed ROIs. Unsupervised clustering of the merged ROI dataset identified 15 transcriptionally distinct cell populations (Fig. 3B and sFig. 2D). The lymphocyte and myeloid_Cell_1/2 populations were further resolved by secondary clustering analyses to

improve cellular annotation. Notably, eosinophils and ILC2s, which we previously identified as key components of dermal TRM-dependent type 2 immune niches, were not recovered as distinct transcriptional clusters. Histological examination of matched H&E sections revealed abundant eosinophils within the same inflammatory lesions, readily identifiable by their characteristic bilobed nuclei and eosinophilic cytoplasmic granules (Fig. 3C, insets 1-3). However, these cells were not reconstructed as discrete cellular objects by the transcript-based Baysor segmentation pipeline. We therefore applied an alternative segmentation approach using the nuclear expansion-based Xenium algorithm, which successfully identified nuclei corresponding morphologically to eosinophils (sFig. 3A). However, most of these cells contained fewer than 30 detected transcripts, falling below the transcript threshold used in the Baysor pipeline, and lacked detectable expression of canonical eosinophil-associated genes included in our Xenium panel (sFig. 3B). These findings suggest that, despite their clear histological presence, eosinophils were not reliably captured as transcriptionally defined cell populations in our Xenium dataset. Consistent with this limitation, three clusters (Mast_Fibro_Mixed, T_Fibro_Mixed, and Myeloid_Mixed) displayed mixed transcriptional signatures, most likely reflecting imperfect cell boundary reconstruction by current segmentation algorithms in densely inflamed tissues (Fig. 3B).

Comparison of inflamed and non-inflamed ROIs revealed marked enrichment of inflammatory monocytes, DCs, neutrophils, and T lymphocytes within inflamed ROIs, consistent with a localized type 1 inflammatory response (Fig. 3B, right panel). Differential expression analysis identified strong enrichment of IFNγ-responsive genes, including *Cxcl9*, *Cxcl10*, *Stat1*, *Gbp5*, *Nos2*, and *Tgtp2*, within inflamed ROIs (sFig. 2E). Gene Ontology analysis also demonstrated significant enrichment of pathways involved in leukocyte activation, migration, cytokine signaling, and immune cell interactions in inflamed ROIs, whereas non-inflamed ROIs were enriched for pathways associated with tissue homeostasis, lipid metabolism, and tissue repair (sFig. 2F).

To determine the spatial relationship between parasite persistence and local immune organization, UMAP-derived cell annotations were projected back onto tissue coordinates together with the locations of parasite transcripts within each ROI (Fig. 4A and sFig. 4). Cells assigned transcripts from two or more independently detected LmFn genes (Lm≥2-positive cells) were classified as high-confidence parasite-associated cells. The majority of these cells were annotated as Inflammatory_Monocytes, Dermal_TRM/TRM_Like, and Myeloid_Mixed populations (Fig. 4C, left panel). Because parasite transcripts were sparse and cell-boundary reconstruction remains imperfect in densely inflamed tissues, these assignments may include both parasite-containing cells and neighboring cells to which parasite transcripts were incorrectly assigned. Neighborhood analysis within a 100-μm radius centered on each Lm≥2-positive cell revealed enrichment of inflammatory monocytes, neutrophils, and $CD4^+$ and $CD8\alpha^+$ T cells (Fig. 4C, right panel). Despite this local accumulation of inflammatory cells, organized granuloma-like structures were not observed at sites of parasite persistence.

We next asked whether persistent parasites preferentially localized within a type 2 immune microenvironment orchestrated by dermal TRMs. To address this, we calculated type 2 inflammatory niche scores using genes associated with the previously described dermal TRM maintenance circuitry and alternative macrophage activation, including *Il4, Ccl24, Tslp, Arg1,* and *Retnla* [23, 24]. These scores were compared with type 1 inflammatory niche scores derived from type 1 immune genes, including *Tnf*, *Nos2*, *Cxcl9*, *Cxcl10*, *Il12b*, *Ifng*, and *Il27*. Spatial mapping revealed that parasite-associated signals preferentially localized to regions with elevated type 2 inflammatory niche scores and away from areas exhibiting the strongest type 1 inflammatory signatures (Fig. 4B and sFig. 4). In contrast, matched non-inflamed ROIs exhibited neither elevated type 1 inflammatory nor type 2 inflammatory niche scores. Quantitative neighborhood analysis centered on Lm≥2-positive cells across all inflamed ROIs further demonstrated a marked predominance of type 2 inflammatory over type 1 inflammatory niche

signals (Fig. 4D). Together, these analyses demonstrate that parasite-associated signals preferentially localize to spatially restricted type 2 inflammatory tissue domains embedded within broader IFNγ-dominated inflammatory foci.

L. major persistence is abrogated in mice with conditional deficiencies in type 2 cytokines.

To further investigate the role of dermal TRMs in sustaining *L. major* infection after clinical healing, we studied *L. major* persistence following healing in a series of mouse strains with conditional immune deficiencies previously shown to compromise the number and M2-like activation state of the dermal TRMs during infection [23, 24]. *EoCre:IL4/13$^{f/f}$* mice, which lack IL-4/IL-13 production from eosinophils, achieved an 80% clinical healing rate by 24 weeks post-infection, similar to the WT B/6 controls (Fig. 5A and sFig5. A and B). Notably, *eoCre:IL4/13$^{f/f}$* mice developed slightly larger lesions with more severe pathology compared to WT mice during weeks 7 - 10 post-infection. At 11 weeks post-infection, the parasite burdens in *eoCre:IL4/13$^{f/f}$* mice were 25-fold lower than in controls, with no *ex vivo* recovery of parasites from two of the *eoCre:IL4/13$^{f/f}$* mice (Fig. 5B). Flow cytometric analysis of the cells recovered from the ear revealed increased production of IFNγ and TNFα from T cells in *eoCre:IL4/13$^{f/f}$* mice compared to WT controls (Fig. 5C). As previously reported [23], the numbers of TRMs and eosinophils were significantly decreased in *eoCre:IL4/13$^{f/f}$* mice, while the numbers of infiltrating PMNs, monocytes, and moDCs, were significantly increased (Fig. 5D).

At 24 weeks post-infection, persisting parasite burdens in the ears and draining lymph nodes (dLN) of clinically healed *eoCre:IL4/13$^{f/f}$* mice were 265-fold and 7-fold lower, respectively, compared to WT controls (Fig. 5E). Importantly, 8 out of 20 ears and 12 out of 20 dLNs from *eoCre:IL4/13$^{f/f}$* mice showed no parasite growth *ex vivo*, compared to 0 out of 20 ears and 6 out of 20 dLNs from WT controls. We also quantified parasite DNA to measure the combined burdens of dying/dead and live parasites. WT-healed ears contained 20,000-fold

greater parasite DNA than *eoCre:IL4/13*$^{f/f}$ ears, with 14 out of 20 *eoCre:IL4/13*$^{f/f}$ ears failing to amplify any parasite DNA compared to 1 out of 16 WT ears (Fig. 5F).

In addition to IL-4/IL-13 from eosinophils, we previously showed that CCL24 and TSLP from dermal TRMs, as well as IL-5^{+} ILC2s, are necessary to maintain the number and M2-like profile of dermal TRMs during infection [23, 24]. We infected *Ccl24-Cre*^{het}*:Tslp*$^{f/f}$ mice, which selectively lack TSLP production from dermal TRMs based on our finding that *Ccl24-cre* is a highly specific Cre expressor for dermal TRMs. Because *Ccl24-Cre*^{het} mice exhibit a 45% reduction in endogenous *Ccl24* mRNA expression compared to WT [24], we included *Ccl24-Cre*^{het} mice alongside WT B/6 controls. All groups, including *Ccl24-Cre*^{het}*:Tslp*$^{f/f}$, *Ccl24-Cre*^{het}, and WT mice, achieved an approximate 90% clinical healing rate by 23 weeks post-infection (sFig5. C-E). However, *Ccl24-Cre*^{het}*:Tslp*$^{f/f}$ mice developed slightly larger lesions (1 – 1.5 mm larger on average) compared to WT mice during week 7 - 9 post-infection. At 23 weeks p.i., parasite burdens in *Ccl24-Cre*^{het}*:Tslp*$^{f/f}$ and *Ccl24-Cre*^{het} mice were 4,812- and 155-fold lower, respectively, compared to WT controls, with 24 out of 38 *Ccl24-Cre*^{het}*:Tslp*$^{f/f}$ and 3 out of 26 *Ccl24-Cre*^{het} mice failing to grow out parasites from whole ear tissue *ex vivo* (Fig. 5G).

We also infected *R5:Gata3*$^{f/f}$ mice, which have *Il5* linked to Cre recombinase and lack the critical transcription factor Gata3 necessary for the generation of IL-5^{+} ILC2s [24]. *R5:Gata3*$^{f/f}$ and WT mice achieved clinical healing rates of 90% and 75%, respectively, by 24 weeks post-infection (sFig. 5F-H). On average, parasite burdens in the healed *R5:Gata3*$^{f/f}$ mice were 2,230-fold lower compared to the healed WT mice, with no *ex vivo* recovery of parasites from 32 out of 38 ears from the *R5:Gata3*$^{f/f}$ mice, while parasites were recovered from all 40 ears from WT mice (Fig. 5H).

Targeted depletion of dermal TRMs or IL-5 neutralization promotes clearance of residual parasites in healed mice.

To investigate how targeted ablation of M2-like dermal TRMs after clinical healing affects the persistence of *L. major* infection, we used *Ccl24-cre:DTR* mice, which render dermal TRMs susceptible to deletion following diphtheria toxin (DT) administration. Both *Ccl24-cre:DTR* and WT mice achieved clinical healing rates of 72% and 69%, respectively, by 24 weeks post-infection (Fig. 6A and sFig. 6A and B). At week 25, 5 days after the first DT administration, we confirmed a significantly reduced number of dermal TRMs in *Ccl24-Cre:DTR* mice, but not in DT treated nor WT controls (Fig. 6B). This reduction was accompanied by increased infiltration of monocytes and neutrophils. Microscopic analysis of infected cells recovered from the same ear samples revealed that the DT-treated *Ccl24-Cre:DTR* group had a significant reduction in the proportion of cells harboring multiple parasites (3-5, 6-10, and >15 parasites per cell), along with a significant increase in cells containing a single parasite, suggesting new infections by parasites released from dying, heavily infected cells (Fig. 6C). The overall parasite burdens were not affected in either *Ccl24-Cre:DTR* or WT mice at week 25 after the first DT administration (Fig. 5D). In consideration of the possibility that prolonged depletion of the dermal TRMs might be required, and/or that the newly infected inflammatory monocyte and moDCs might require additional time to be activated for killing, the mice were treated once a week for 5 consecutive weeks and sacrificed 4 weeks after the last treatment (Fig. 6A). Using this regimen, the DT-treated *Ccl24-cre:DTR* mice showed a 350-fold decrease in average parasite burdens compared to DT-treated WT controls. Moreover, 3 out of 8 ears from DT-treated *Ccl24-cre:DTR* mice showed no parasite growth *ex vivo* (Fig. 6E), while parasites could be grown out from all 14 ears of the DT-treated WT mice.

To evaluate the therapeutic potential of disrupting localized type 2 circuitries post-clinical healing, we selected IL-5 neutralization to inhibit eosinophil maturation and survival. We confirmed that a single intraperitoneal administration of IL-5 neutralizing antibody (TRFK5) effectively depletes eosinophils systemically, including in the ear skin (Fig. 6F). After WT mice reached an 88% clinical healing rate by 24 weeks post-infection, these animals were

304 administered either TRFK5 or control IgG intraperitoneally once a week for 8 consecutive
305 weeks. One week after the final treatment, TRFK5-treated mice exhibited a 10-fold reduction in
306 average parasite burden compared to IgG-treated WT controls. Notably, parasites could not be
307 recovered *ex vivo* from 6 out of 18 ears in the TRFK5-treated group, whereas all 18 ears from
308 IgG-treated WT controls yielded viable parasites (Fig. 6H). As shown previously (Fig. 5H),
309 healed *R5:Gata3*$^{f/f}$ mice exhibited a 352-fold lower parasite burden relative to IgG-treated WT
310 controls, with no *ex vivo* parasite recovery from 17 out of 18 ears.
311
312
313 **Discussion**
314 *Leishmania* persistence following clinical healing is a hallmark of leishmanial infections,
315 placing the host at risk of disease reactivation and greatly contributing to the pool of infection
316 reservoirs. Prior studies of *Leishmania* persistence have focused largely on cutaneous
317 leishmaniasis and identifying the tissues and host cell populations that harbor residual parasites
318 after healing. Although fibroblasts, adipocytes, and other non-canonical host cells have been
319 proposed as potential reservoirs because of their intrinsically poor microbicidal capacity,
320 definitive evidence supporting their role in maintaining infection in healed skin remains limited [19,
321 20, 21]. Our findings identify dermal TRMs as the predominant host cells supporting parasite
322 persistence. Using multiplex imaging and high-resolution spatial transcriptomics, we provide the
323 first direct visualization of persistent parasites in the skin and offer a spatial framework for
324 understanding how dermal TRMs enable parasite survival despite otherwise effective immunity.
325 We show that parasites are localized to small, discrete inflammatory foci characterized by
326 infiltrating monocytes, neutrophils, and T cells, but that within these foci they are preferentially
327 concentrated within microdomains enriched for type 2 and dermal TRM-associated molecules.
328 These observations support a model in which a balance between parasite growth and

containment is maintained by infection of dermal TRMs that provide a spatially restricted replicative niche nested within a T_H1-mediated inflammatory environment.

A B/6 mouse with a healed *L. major* infection is widely considered a classical infection-driven model of T_H1 dominance, exhibiting strong and durable immunity to reinfection. Our findings indicate that the small, inflamed regions in which the persisting parasites are found reflect an ongoing T_H1 response, containing inflammatory monocytes, neutrophils, $CD4^+$ and $CD8\alpha^+$ T cells, and exhibiting strong IFNγ-inducible transcriptional programs. Parasite survival within this type 1 inflammatory setting is a remarkable feature of the persistence phenotype. We could find no evidence for granulomatous structures that might sequester them from damage. Instead, their residence within dermal TRMs that maintain an alternatively activated state is key to their persistence. Several other features of dermal TRMs make them particularly well suited to serve as long-term reservoirs for *L. major*. Dermal TRMs are embryonically derived, long-lived, largely sessile cells that occupy stable niches within the skin [22, 28, 29]. Their capacity for long-term retention is perhaps best illustrated by the biology of tattoos, in which dermal macrophages repeatedly capture, release, and recapture pigment while maintaining its location throughout adult life [30].

Our conclusion that dermal TRMs harbor the majority of persistent *L. major* is based on the number of viable parasites found within sorted populations of myeloid cells recovered from healed skin, and by multiplex imaging that revealed that high intracellular parasite loads were confined to the dermal TRMs. By contrast, the identity of the infected cells was more difficult to accurately discern from the Xenium spatial analysis. While this analysis assigned parasite-associated transcripts to inflammatory monocytes, dermal TRM/TRM-like cells, and other myeloid cells, these cellular assignments should be interpreted cautiously. Parasite transcripts were sparse, and cell-boundary reconstruction remains challenging in densely inflamed tissues, particularly among closely apposed myeloid cells. Consequently, some parasite transcripts may have been assigned to cells neighboring the actual infected host cell. In addition, some cell

types were completely absent from the dataset annotations. Complementary histological and confocal analyses demonstrated eosinophil infiltration at these sites, consistent with our previous finding that eosinophils support dermal TRM maintenance by providing a local source of IL-4 [23]. Although eosinophils were not recovered as a discrete population in the Xenium dataset, matched histological sections revealed abundant eosinophils within the same inflammatory foci, indicating that their underrepresentation likely reflected the low transcript content of these cells under the panel and segmentation conditions used in this study. ILC2s were also not identified as a distinct cluster, likely because the restricted gene content of the custom panel did not include sufficient markers to confidently distinguish lineage-negative innate lymphocyte populations.

Despite these limitations in cellular resolution and representation, the Xenium spatial analysis was informative for defining the broader immune architecture surrounding sites of persistence. Parasite signals consistently localized within tissue microdomains enriched for expression of dermal TRM and other type 2 associated genes, including *Ccl24 (eotaxin 2)*, *Tslp*, *Il4*, *Arg1*, and *Retnla*, which were embedded within a broader IFNγ-dominated inflammatory milieu. This spatial segregation of permissive and microbicidal programs provides a structural explanation for how persistent parasites survive despite robust type 1 immunity. More broadly, our findings illustrate the utility of spatial transcriptomics to reveal the local immune landscape of infection even when pathogen transcript recovery is limited, and when cellular segmentation / identities within inflamed tissue are difficult to accurately resolve.

Our imaging and genetic studies further support a model in which relatively low numbers of parasites are maintained through a dynamic balance between replication and immune-mediated destruction. While the dermal TRMs represented the most heavily parasitized cells within healed lesions, monocytes and monocyte-derived cells typically contained fewer or only a single organism. Consistent with our previous observations in active lesions [22], dermal TRMs remained iNOS-negative, whereas infected monocyte-derived cells were frequently iNOS-

positive. These findings suggest that parasite replication is largely restricted to dermal TRMs, while parasites released into the surrounding inflammatory environment are phagocytosed by monocyte-derived cells that are subject to IFNγ-dependent activation. This interpretation is supported by our DT-mediated depletion studies, in which selective elimination of dermal TRMs in healed mice reduced the frequency of heavily infected cells while transiently increasing the proportion of cells containing only a single parasite. The ability of the dermal TRM depletion to actually reduce parasite burdens in healed mice became apparent only after repeated DT treatments and an extended observation period, suggesting that following release of viable parasites from toxified TRMs, the newly infected cells required time to acquire full leishmanicidal capacity.

A balance of *L. major* replication and destruction has been previously proposed to explain the persistence of low numbers of organisms following healing in the footpad, with the critical difference that in the sub-cutaneous footpad site the replicating parasites were observed within both iNOS-positive and iNOS-negative populations of infected cells [31]. While these studies did not directly address the ontogenic heterogeneity of the cells, neither Relmα$^+$ nor CD206$^+$ populations, both markers of dermal TRMs, were observed harboring persisting parasites. This discrepancy may reflect differences in the resident macrophage populations present at distinct anatomical sites within the skin and underlying tissues. Unlike the dermis, which contains abundant lymphoid cells and a dense network of dermal TRMs, the hypodermis is dominated by CD11b$^+$ myeloid cells and contains transcriptionally distinct hypodermal TRMs [32].

The tightly regulated balance between *L. major* survival and killing in the healed site is evident from the rapid reactivation of disease following inhibition of CD4$^+$ or CD8α$^+$ T cells, IL-12, INFγ, or iNOS on the one hand [15, 16, 17], and reduced numbers of residual parasites in mice with the conditional deficiencies in type 2 responses required for dermal TRM maintenance

shown here on the other. Thus, mice lacking eosinophil-derived IL-4/IL-13, ILC2-derived IL-5, or TRM-derived TSLP, each developed and resolved lesions with kinetics similar to WT controls, yet exhibited dramatically reduced parasite burdens, including the absence of detectable parasites after healing. Because each of these immune deficits reduces dermal TRM abundance and impairs maintenance of their M2-like activation state [23, 24], these findings establish a direct relationship between dermal TRM biology and parasite persistence.

The therapeutic implications of these findings was tested by systemic IL-5 neutralization, which promoted reduced numbers of residual parasites, including their complete clearance, in mice treated post-healing. Multiple drugs, including mepolizumab/reslizumab (anti-IL5 antibodies) and benralizumab (an anti-IL5Rα antibody), are already approved for clinical use in various eosinophil related pathologies and possess well-established safety profiles [33, 34, 35]. Repurposing these drugs to treat Leishmania patients post clinical healing, or as adjunct therapy during treatment of active disease, may represent a strategy for achieving sterile cure.

Acknowledgements: We thank Dr. Erin F. McCaffery for her expertise and guidance in spatial transcriptomic data analysis and Dr. Amy Klion for her expertise in the histological identification of eosinophils in H&E-stained tissue sections.

Funding: This work was supported in part by the Intramural Research Program of the National Institute of Allergy and Infectious Diseases, National Institutes of Health.

Author contributions: S.H.L. and D.L.S. designed the study. S.H.L., T.Z.V., O.K., and M.S. performed experiments. S.H.L. and T.R.F. analyzed the data. S.H.L. and D.L.S. wrote the manuscript.

Competing interests: The authors declare no competing interests.

Materials and Methods

Mice

C57BL/6 (B/6) mice were procured from Taconic Farms. *B6(C)-Il5*$^{tm1.1(icre)Lky}$*/J* (*R5*) and *C57BL/6-Gt(ROSA)26Sor*$^{tm1(HBEGF)Awai}$*/J* (*DTR*), and *Gata3tm1.1Mbu*/J (*Gata3*$^{f/f}$) mice were obtained from The Jackson Laboratory. The *eoCre:IL4/13*$^{f/f}$ mice on a C57BL/6 background were acquired as previously described [23]. Additionally, *Ccl24-IRES-Cre* (*Ccl24-Cre*) and *Tslp*$^{f/f}$ mice were generated as previously reported [24]. All mice used in these studies were female, aged 6-8 weeks, and were bred and/or maintained in the NIAID animal care facility under specific pathogen-free conditions. The use of these animals was carried out in accordance with a study protocol approved by the NIAID Animal Care and Use Committee (protocol number LPD 68E). Compliance with the Animal Welfare Act, PHS Policy, U.S. Government Principles for the Utilization and Care of Vertebrate Animals Used in Testing, Research, and Training, and the NIH Guide for the Care and Use of Laboratory Animals was strictly adhered to.

In vivo injections

For targeted depletion of dermal TRMs, *Ccl24-Cre:DTR* animals were injected intradermally with 20 ng of diphtheria toxin (DT) in PBS (D0564, Millipore Sigma) once a week for 5 consecutive weeks. To achieve systemic IL-5 neutralization, WT B/6 mice were administered 25 μg of anti-IL-5 antibody (TRFK5, Bio X Cell) *via* intraperitoneal injection once a week for 8 consecutive weeks.

Leishmania major infection

The *L. major* Friedlin V1 (LmFn) strain was cultured under the following conditions: Promastigotes were incubated at 26°C in Medium 199, supplemented with 20% heat-inactivated fetal calf serum (FCS) (Gemini Bio-Products), 100 U/mL penicillin, 100 μg/mL streptomycin, 2 mM L-glutamine, 40 mM Hepes, 0.1 mM adenine (dissolved in 50 mM Hepes), 5 mg/mL hemin (dissolved in 50% triethanolamine), and 1 mg/mL 6-biotin (M199/S). Infective-stage metacyclic promastigotes were obtained from stationary phase cultures (5–6 days) by density gradient centrifugation, as described previously [36]. Mice were inoculated intradermally in the ear dermis with metacyclic promastigotes in a 10 μL volume. Lesion development was tracked weekly by measuring the diameter of ear nodules with a direct-reading Vernier caliper (Thomas Scientific). Lesion pathology was assessed and scored as follows: 0 = no ulceration, 1 = ulcer, 2 = half ear eroded, 3 = entire ear eroded.

Limiting dilution assay for quantification of *L. major*

Ear tissue was prepared as previously described [37]. Briefly, the two sheets of the infected ear dermis were separated and placed in DMEM containing 0.2 mg/mL Liberase TL purified enzyme blend (Roche Diagnostics Corp.). The samples were then incubated for 1.5 hours at 37°C. Following incubation, the digested tissue was processed using a tissue homogenizer for 3.5 minutes (Medi-machine; Becton Dickinson) and filtered through a 70 μm cell strainer (Falcon Products) to obtain a single-cell suspension. Parasite titrations were conducted as previously described [38]. In brief, tissue homogenates were serially diluted in 96-well flat-bottom microtiter plates containing 100 μL M199/S. The number of viable parasites in each ear was determined from the highest dilution at which promastigotes could grow after 7–10 days of incubation at 26°C.

Real-time PCR assay for quantification of *L. major* parasite burden

Quantitative PCR was performed to amplify a single-copy housekeeping gene, Leishmania RNA binding protein (Drbd3), using the following primers: Forward Primer (5'-GCCGCGTGTACATTCGTTTT-3') and Reverse Primer (5'-CTGGTACACGATCTCTGGCG-3'), as previously described [39]. DNA was isolated from whole mouse ear tissues using DNeasy Blood & Tissue kits (Cat# 69504; QIAGEN), and 100 ng of DNA was used per reaction. Each reaction plate contained a standard curve of cultured promastigote DNA, ranging from 1 x 10^7 femtograms (fg) to 100 fg per reaction. PCR reactions were prepared in a final volume of 10 μL, consisting of 5 μL of iTaq universal SYBR Green supermix (Cat# 172-5121; BioRad), 0.5 μL of each primer (1 μM concentration), and 100 ng of genomic DNA per sample. All PCR reactions were performed in triplicate using the QuantStudio12K Flex system (ThermoFisher Scientific). The total parasite DNA was calculated by first using the average Ct value for each reaction to interpolate the fg of parasite DNA per 100 ng of total DNA, relative to the standard curve included on each reaction plate. This DNA (fg per reaction) was then multiplied by the dilution factor used to adjust each sample to 100 ng per PCR reaction, thereby determining the total parasite DNA (fg) per tissue harvested.

Immunolabeling and flow cytometry analysis

Single-cell suspensions were prepared and stained using the LIVE/DEAD Fixable Aqua Dead Cell Stain Kit (ThermoFisher). Cells were incubated with an anti-Fc-γ II/III (CD16/32) receptor antibody (2.4G2, BD Biosciences) in PBS containing 1% FCS, followed by staining with fluorochrome-conjugated antibodies for 1 hour on ice. The following antibodies were used for surface staining: APC anti-mouse CD3 (17A2, Biolegend); Alexa488 anti-mouse TCR β (H57-597, Biolegend); FITC, APC/Cy7, and Brilliant Violet™ 421 anti-mouse Ly6G (1A8, Biolegend); APC/Cy7 anti-mouse Ly6C (HK1.4, Biolegend); FITC and PE/Cy7 anti-mouse CD11b (M1/70, Biolegend); PerCP/Cy5.5, Brilliant Violet™ 421, and APC/Cy7 anti-mouse NK1.1 (PK136,

Biolegend); Alexa647 and APC anti-mouse CD206 (C068C2, Biolegend); PE and Brilliant Violet™ 421 anti-mouse SiglecF (E50-2440, BD Biosciences); APC and APC/Cy7 anti-mouse F4/80 (BM8, Biolegend). For intracellular cytokine detection, single-cell suspensions harvested from tissues were cultured in the presence of PMA/Ionomycin and Brefeldin A (Biolegend) for 4 hours at 37°C. Cells were first stained with the LIVE/DEAD Fixable Aqua Dead Cell Stain Kit (ThermoFisher), followed by surface marker staining, fixation, and permeabilization using BD Cytofix/Cytoperm (BD Biosciences). Subsequently, cells were stained for cytokine/chemokine detection for 30 minutes on ice. The following antibodies were used for intracellular staining: FITC anti-mouse IFNγ (XMG1.2, Biolegend); PerCP-eFluor™710 anti-mouse TNFα (MP6-XT22, Thermo-Fisher Scientific). Data were collected using FacsDIVA software and a FacsCANTO II flow cytometer (BD Biosciences) and analyzed with FlowJo software (Tree Star).

IBEX (Iterative bleaching extends multiplexity) assay

Tissue processing, antibody validation and panel design, and manual IBEX were performed as previously reported [26]. Ears from clinically healed WT animals at 24 weeks post infection were harvested and immediately fixed in 4% formaldehyde at 4°C for 24 hours followed by incubation in 30% sucrose (wt/vol) at 4°C for 24 hours. Ears were embedded in Tissue-Tek OCT (Sakura Finetek). Cryostat cut sections (7 μm) were placed onto Superfrost Plus microscope slides (Fisher Scientific) and dried overnight at room temperature (RT). After rehydrated in PBS for 5 minutes at RT, tissue sections were blocked with PBS containing 0.3% Triton-X-100 (Cat# 93443 Millipore Sigma), 1% bovine serum albumin (Cat# A1933, Millipore Sigma), and 1:100 diluted TruStain FcXTM (93, Biolegend) in PELCO BioWave® Pro+ microwave (36500-230, Ted Pella Inc) on a cooling plate set to 26°C with one cycle of the microwave program (100 watt for 2min - 0 watt for 1min - 100 watt for 2min - 0 watt for 1min - 100 watt for 2min - 0 watt for 1min - 100 watt for 2min - 0 watt for 1min - 100 watt for 2min). Sections were subsequently stained with 100 μl of primary antibody solution with two microwave

cycles and washed with three exchanges of PBS. The slides were mounted with Fluoromount-G (Cat# 0100-01, Southern Biotech) and equilibrated for 30 minutes at RT in the dark. The sample images were acquired with a Leica SP8 confocal laser fluorescence microscope and Imaris software (Bitplane). After manually removing cover slides and washed with PBS, the slides were bleached with a freshly prepared 1 mg/mL $LiBH_4$ solution (Cat#93-0397, STREM Chemicals) for 10 minutes at RT and washed with PBS three times. This labeling, image acquisition, and bleaching were repeated 3 more times for a total of 4 antibody panels (4 parameters per a panel). Four series of 3D image stacks, collected separately in each cycle, were aligned using SimpleITK, previously reported as an intensity-based image alignment protocol to register 3D IBEX-generated images [40]. The following antibodies were used for surface staining: Cycle1 - Alexa488 anti-mouse CD206 (C068C2, Biolegend), Alexa555 anti-*L. major* (generated in-house), iFluor594 anti-mouse iNOS (W16030C, Biolegend), Alexa647 anti-mouse SiglecF (E50-2440, BD Biosciences); Cycle 2 - Alexa488 anti-mouse CD8α (53-6.7, Biolegend), Alexa555 anti-mouse CD11c (N418, Biolegend), iFluor594 anti-mouse IFNγ (XMG1.2., ThermoFisher Scientific), Alexa647 anti-mouse CD4 (Gk1.5, Biolegend); Cycle 3 - Alexa488 anti-mouse CX3CR1 (SA011F11, Biolegend), Alexa555 anti-mouse MPO (AF3667, R&D Systems), iFluor594 anti-mouse IFNγ (BM8, ThermoFisher Scientific), Alexa647 anti-mouse TCR$\gamma\delta$ (GL3, Biolegend); Cycle 4 - Alexa488 anti-mouse CD11b (M1/70, Biolegend), Alexa555 anti-mouse c-Kit (2B8, Biolegend), iFluor594 anti-mouse CD31 (MEC13.3, Biolegend), Alexa647 anti-mouse Tubulinβ3 (TUJ1, Biolegend).

Xenium *in situ* analysis

The Xenium in situ platform (10x Genomics) was used to perform spatially resolved transcriptomic profiling of *Leishmania major*-infected tissue. A Xenium Standalone Custom

Gene Panel comprising 742 murine genes and 10 *L. major* genes was designed based on prior single-cell RNA sequencing datasets of infected C57BL/6 ear tissues [24].

Formalin-fixed paraffin-embedded (FFPE) tissue sections (5 μm) were mounted onto Xenium slides with technical support from Histoserv, Inc. Sections were deparaffinized and permeabilized to allow access to mRNA, followed by overnight probe hybridization at 50°C. After stringency washes to remove unbound probes, probe ligation was performed at 37°C for 2 hours to enable annealing of rolling circle amplification (RCA) primers. Circularized probes were then amplified *via* RCA at 37°C for 2 hours, generating amplified barcode signals for each RNA molecule. Following amplification, background fluorescence was chemically quenched, and slides were loaded into the Xenium Analyzer (10x Genomics) with technical support from Psomagen, Inc. The instrument performed automated cyclic imaging, during which fluorescently labeled probes hybridized to barcode sequences, followed by imaging and probe removal. This process was repeated across multiple cycles and channels. Z-stack images were acquired and computationally stitched across fields of view (FOVs) to reconstruct a full spatial representation of transcript localization. Puncta corresponding to individual RNA molecules were detected, filtered, and decoded using a Xenium codebook through a probabilistic maximum likelihood framework.

To improve cell segmentation accuracy beyond vendor-provided boundaries, a custom segmentation pipeline was implemented. High-resolution morphology images (morphology focus channel) were extracted and processed using the StarDist deep learning model (2D_versatile_fluo) for nucleus/cell seed detection. Due to the large size of Xenium images, segmentation was performed in a tiled manner (2048 × 2048 pixels), and tile-wise predictions were subsequently merged into full-resolution segmentation masks. Unique label offsets were applied during merging to ensure non-overlapping cell identities across tiles. Transcript coordinates were converted from micron space to pixel space using the Xenium spatial scaling factor (0.2125 μm per pixel). The Baysor algorithm (v0.7.1) was used to refine cell segmentation

by integrating transcript density with prior segmentation masks generated from StarDist. Baysor was run with the following parameters: --scale 12, --min-molecules-per-cell 30, and --prior-segmentation-confidence 0.7. This approach allowed probabilistic reassignment of transcripts to cells and improved segmentation accuracy, particularly in densely packed or low-RNA cell populations. Four independent Xenium regions were processed separately using identical pipelines (StarDist → Baysor). For each region, Baysor outputs including cell boundaries, segmentation maps, and count matrices were generated. Region-specific Seurat objects were constructed from Baysor-derived count matrices and cell metadata. Following individual processing, regions were merged into a combined Seurat object for downstream analysis. To focus on biologically relevant areas, regions of interest (ROIs) corresponding to micro-infection foci were manually selected based on spatial clustering of *L. major* transcripts and chemokine expression (e.g., *Cxcl9*). ROI selection was performed using coordinate-based cropping or interactive selection.

Statistical analyses

The differences in values obtained for two different groups were determined using the non-parametric Mann-Whitney test. For comparisons of multiple groups, one-way analysis of variance (ANOVA) followed by Dunn's post-test was used. Analyses were performed using Prism 8.0 software (GraphPad).

Figure1

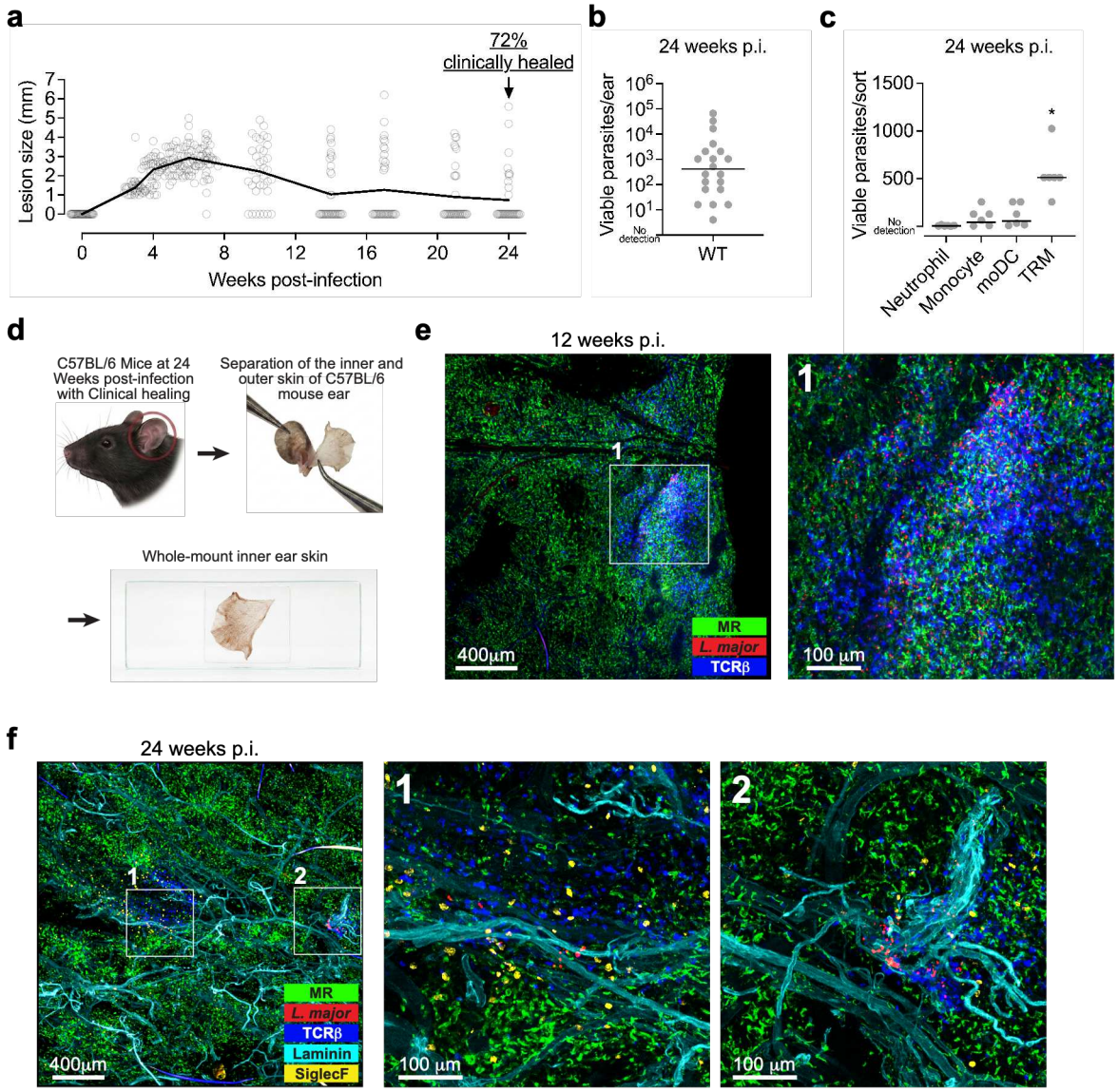


Figure 1. Dermal tissue-resident macrophages are the principal host cells harboring persistent *L. major* after clinical healing in B/6 mice.

(A) Clinical course of infection following intradermal inoculation of 1 × 10^3 *L. major* Friedlin (LmFn) metacyclic promastigotes into the ear dermis, showing lesion development and subsequent clinical healing by 24 weeks post-infection. Each symbol represents an individual ear measurement at the indicated time point; the line connects mean values. **(B)** Viable parasite burdens in clinically healed ears at 24 weeks post-infection, as determined by limiting dilution

assay. Data are shown as individual values and geometric means. **(C)** Viable parasite burdens in the indicated flow cytometry-sorted cell populations isolated from whole clinically healed ears of an independent cohort of WT mice at 24 weeks post-infection, as determined by limiting dilution assay. Data are shown as individual values and geometric means. *$P < 0.05$. **(D)** Schematic illustrating the preparation of anterior ear skin whole mounts for three-dimensional imaging of persistent infection sites in clinically healed B/6 mice. **(E, F)** Whole-mount immunofluorescence imaging of inner ear skin from B/6 mice during lesion regression at 12 weeks post-infection (E) and following clinical healing at 24 weeks post-infection (F). Boxed regions are shown at higher magnification in the corresponding numbered panels. Scale bars, 400 μm (overview images) and 100 μm (magnified regions).

Figure2

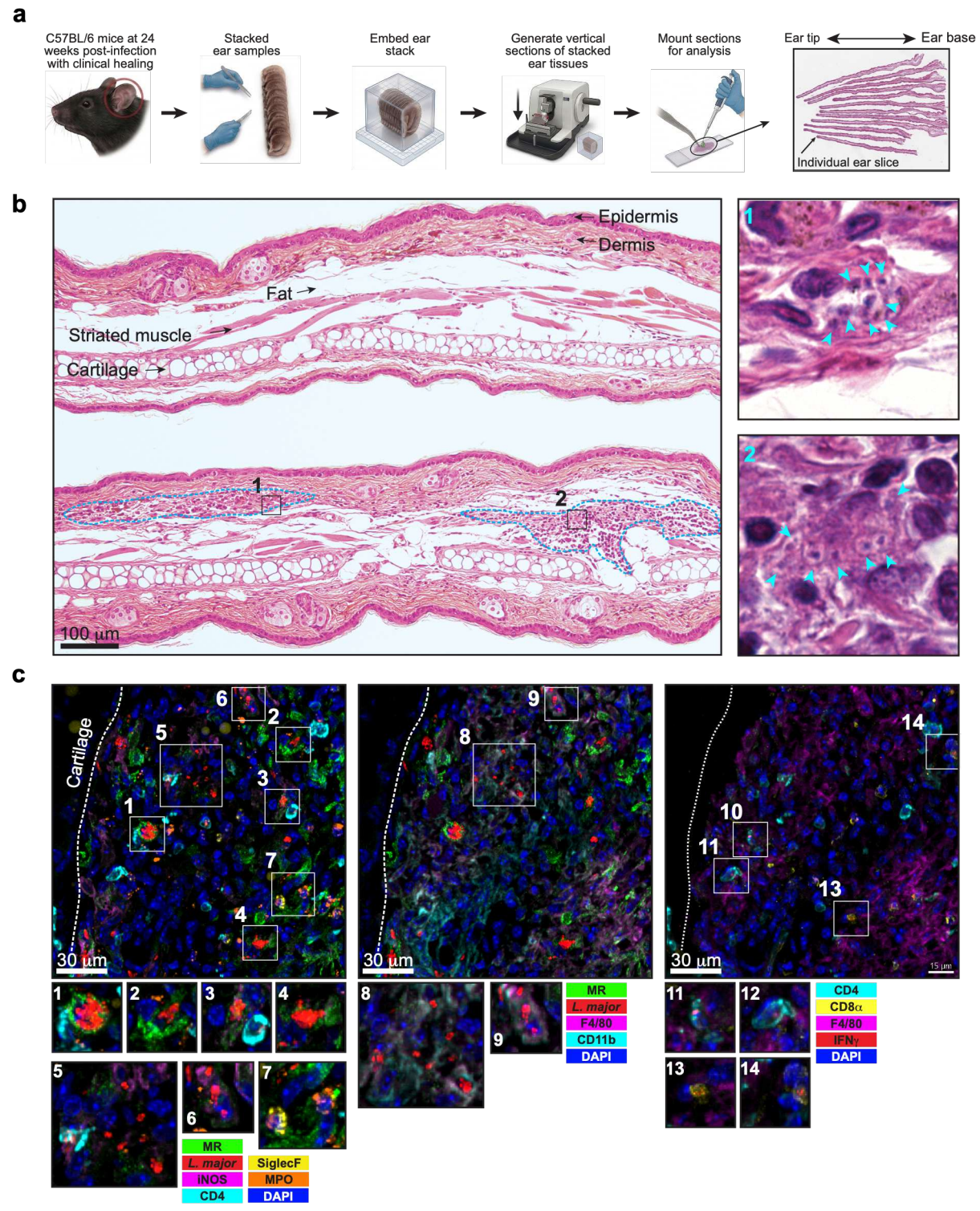


Figure 2. Cellular organization of persistent infection sites in clinically healed B/6 mice.

(A) Schematic illustrating the generation of serial vertical sections from stacked ears collected from clinically healed B/6 mice at 24 weeks post-infection. Sections were oriented on the slide left to right corresponding to ear tip to ear base adjacent to the skull. **(B)** Hematoxylin and eosin (H&E) staining of vertical ear sections from clinically healed WT B/6 mice at 24 weeks post-infection. The cyan dotted line delineates a focal region of immune cell infiltration. Boxed regions 1 and 2 are shown at higher magnification. Cyan arrowheads indicate intracellular amastigotes. **(C)** Multiplexed immunofluorescence imaging by Iterative Bleaching Extends Multiplexity (IBEX) of vertical ear sections containing persistent parasites at 24 weeks post-infection. Four staining cycles were performed, and 12 of the 16 analyzed markers are shown. Numbered boxes are shown at higher magnification below the corresponding images. The white dotted line delineates the cartilage. Data are representative of two independent experiments.

Figure3

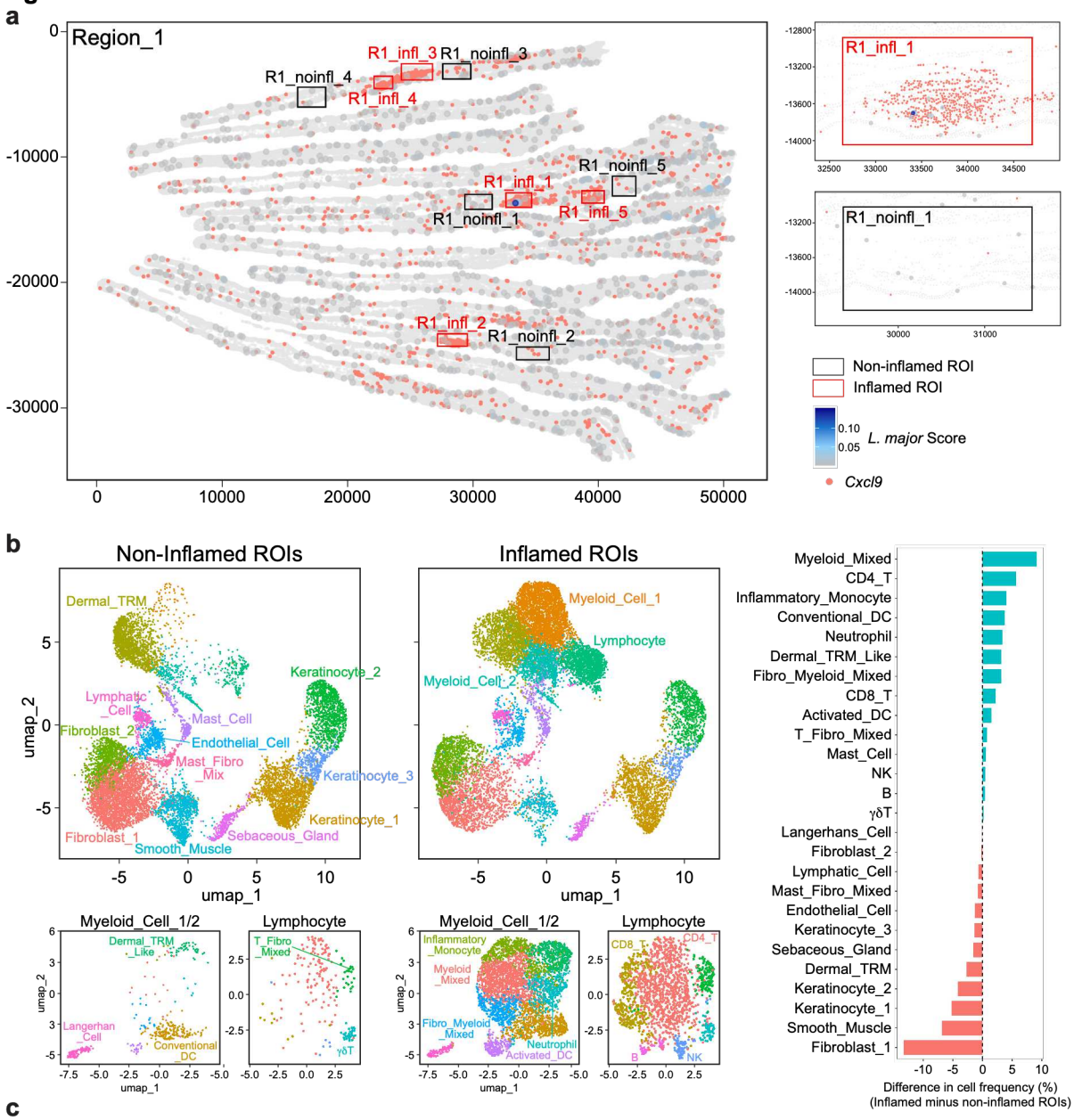

a
Region_1
R1_infl_3
R1_noinfl_3
R1_noinfl_4
R1_infl_4
R1_noinfl_5
R1_infl_1
R1_noinfl_1
R1_infl_5
R1_infl_2
R1_noinfl_2
R1_infl_1
R1_noinfl_1
Non-inflamed ROI
Inflamed ROI
0.10
0.05
L. major Score
Cxcl9
b
Non-Inflamed ROIs
Inflamed ROIs
Dermal_TRM
Lymphatic_Cell
Fibroblast_2
Mast_Cell
Endothelial_Cell
Mast_Fibro_Mix
Keratinocyte_2
Keratinocyte_3
Keratinocyte_1
Fibroblast_1
Smooth_Muscle
Sebaceous_Gland
Myeloid_Cell_1
Lymphocyte
Myeloid_Cell_2
umap_1
umap_2
Myeloid_Cell_1/2
Lymphocyte
Dermal_TRM_Like
Langerhan_Cell
Conventional_DC
T_Fibro_Mixed
γδT
Inflammatory_Monocyte
Myeloid_Mixed
Fibro_Myeloid_Mixed
Neutrophil
Activated_DC
CD8_T
CD4_T
B
NK
Myeloid_Mixed
CD4_T
Inflammatory_Monocyte
Conventional_DC
Neutrophil
Dermal_TRM_Like
Fibro_Myeloid_Mixed
CD8_T
Activated_DC
T_Fibro_Mixed
Mast_Cell
NK
B
γδT
Langerhans_Cell
Fibroblast_2
Lymphatic_Cell
Mast_Fibro_Mixed
Endothelial_Cell
Keratinocyte_3
Sebaceous_Gland
Dermal_TRM
Keratinocyte_2
Keratinocyte_1
Smooth_Muscle
Fibroblast_1
Difference in cell frequency (%)
(Inflamed minus non-inflamed ROIs)
c
Baysor cell boundary overlay on H&E image (R2_infl_2)

Figure 3. Spatial transcriptomic analysis defines the cellular composition of persistent infection-associated inflammatory foci.

(A) Spatial mapping of *Cxcl9* expression and weighted *L. major* parasite-density scores in a representative Xenium section (Region 1) from clinically healed B/6 mice at 24 weeks post-infection. Four Xenium sections (Regions 1 - 4), comprising two sections from each of two independently prepared tissue blocks containing 12 stacked ears per block, were analyzed. Regions of interest (ROIs) exhibiting focal *Cxcl9* expression were designated as inflamed ROIs (red boxes), whereas adjacent *Cxcl9*-low regions were selected as matched non-inflamed ROIs (black boxes). Enlarged panels show a representative inflamed ROI (R1_infl_1) containing focal *Cxcl9* expression and parasite-associated signals and its matched non-inflamed ROI (R1_noinfl_1). **(B)** UMAP visualization of cells within inflamed and matched non-inflamed ROIs following StarDist-Baysor segmentation and unsupervised clustering. Major cell populations are indicated. Lymphocyte and Myeloid_Cell_1/2 populations were further resolved by secondary clustering, as shown in the lower UMAPs. The right panel shows differences in the relative abundance of each cell type between inflamed and matched non-inflamed ROIs, expressed as the percentage in inflamed ROIs minus the percentage in non-inflamed ROIs. **(C)** Representative H&E image of an inflamed ROI (R2_infl_2) overlaid with Baysor-derived cell boundaries. Boxed regions are shown at higher magnification. Green circles indicate morphologically identified eosinophils with characteristic bilobed nuclei and eosinophilic cytoplasmic granules that were not reconstructed as discrete cellular objects by the Baysor segmentation pipeline.

Figure4

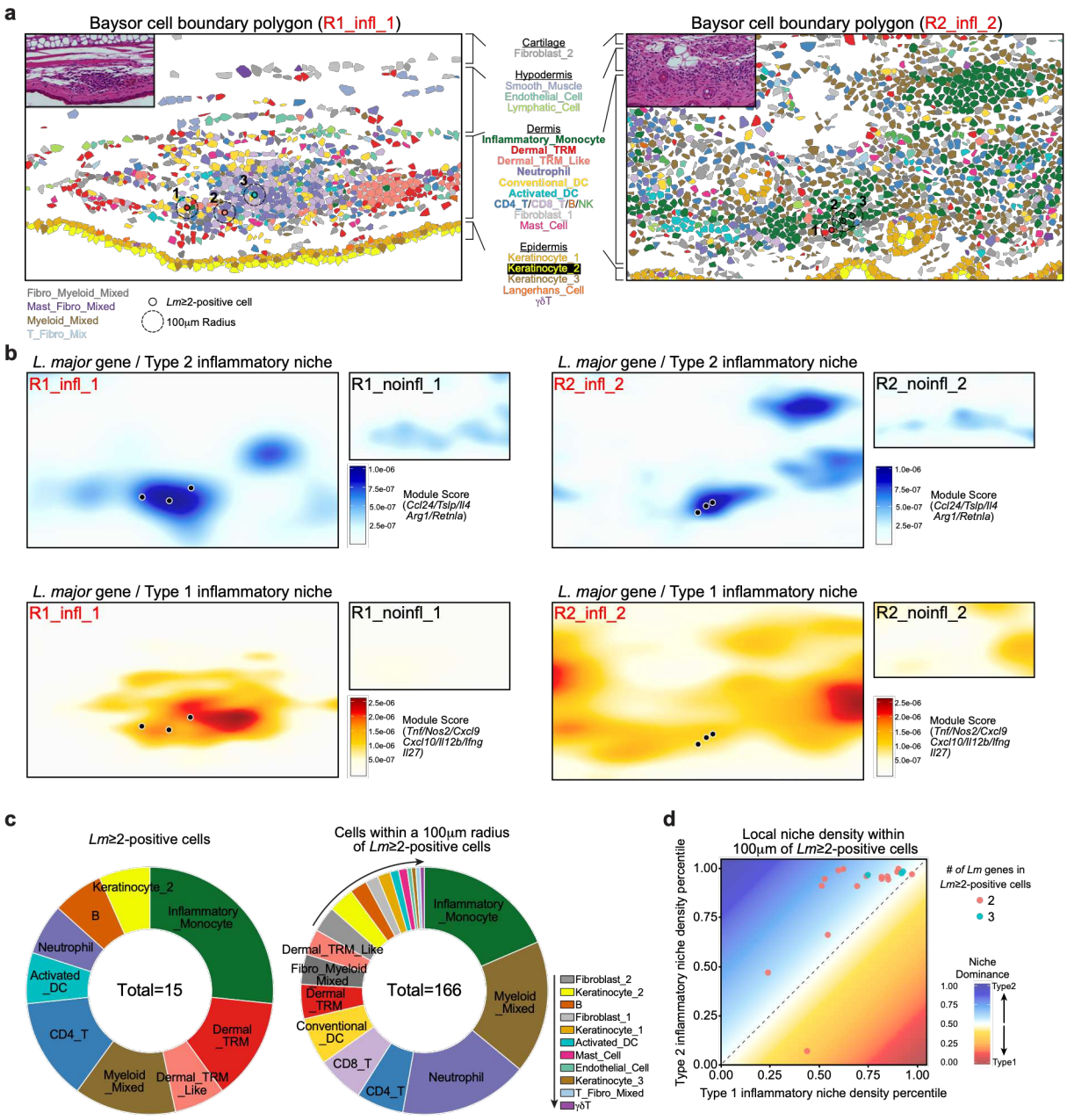


Figure 4. Persistent *L. major* localizes to dermal TRM- and Type 2-associated niches embedded within inflammatory foci.

(A) Spatial reconstruction of representative inflamed ROIs from Region 1 (R1_infl_1) and Region 2 (R2_infl_2). Baysor-derived cell segmentation polygons are colored according to cell identity and projected onto their original tissue coordinates. Insets show the corresponding

H&E-stained Xenium sections. Open black circles indicate cells assigned transcripts from two or more independently detected *L. major* genes (Lm≥2-positive cells). Dashed circles indicate 100-μm-radius neighborhoods surrounding individual Lm≥2-positive cells. **(B)** Spatial maps of Type 2 inflammatory niche scores (*Ccl24, Tslp, Il4, Arg1,* and *Retnla*) and Type 1 inflammatory niche scores (*Tnf, Nos2, Cxcl9, Cxcl10, Ifng, Il12b,* and *Il27*) overlaid with Lm≥2-positive cells in representative inflamed ROIs in (A) (R1_infl_1 and R2_infl_2) and their matched non-inflamed ROIs. **(C)** Cell-type composition of Lm≥2-positive cells across all 20 inflamed ROIs (left) and of neighboring cells located within a 100-μm radius of each Lm≥2-positive cell (right). **(D)** Neighborhood analysis comparing Type 2 and Type 1 inflammatory niche densities within a 100-μm radius of individual Lm≥2-positive cells across all inflamed ROIs. Niche densities are expressed as percentiles across the analyzed neighborhoods. Each point represents one Lm≥2-positive cell and is colored according to the number of independently detected *L. major* genes assigned to that cell. Points above the diagonal indicate neighborhoods with relatively greater Type 2 inflammatory niche density, whereas points below the diagonal indicate neighborhoods with relatively greater Type 1 inflammatory niche density.

Figure5

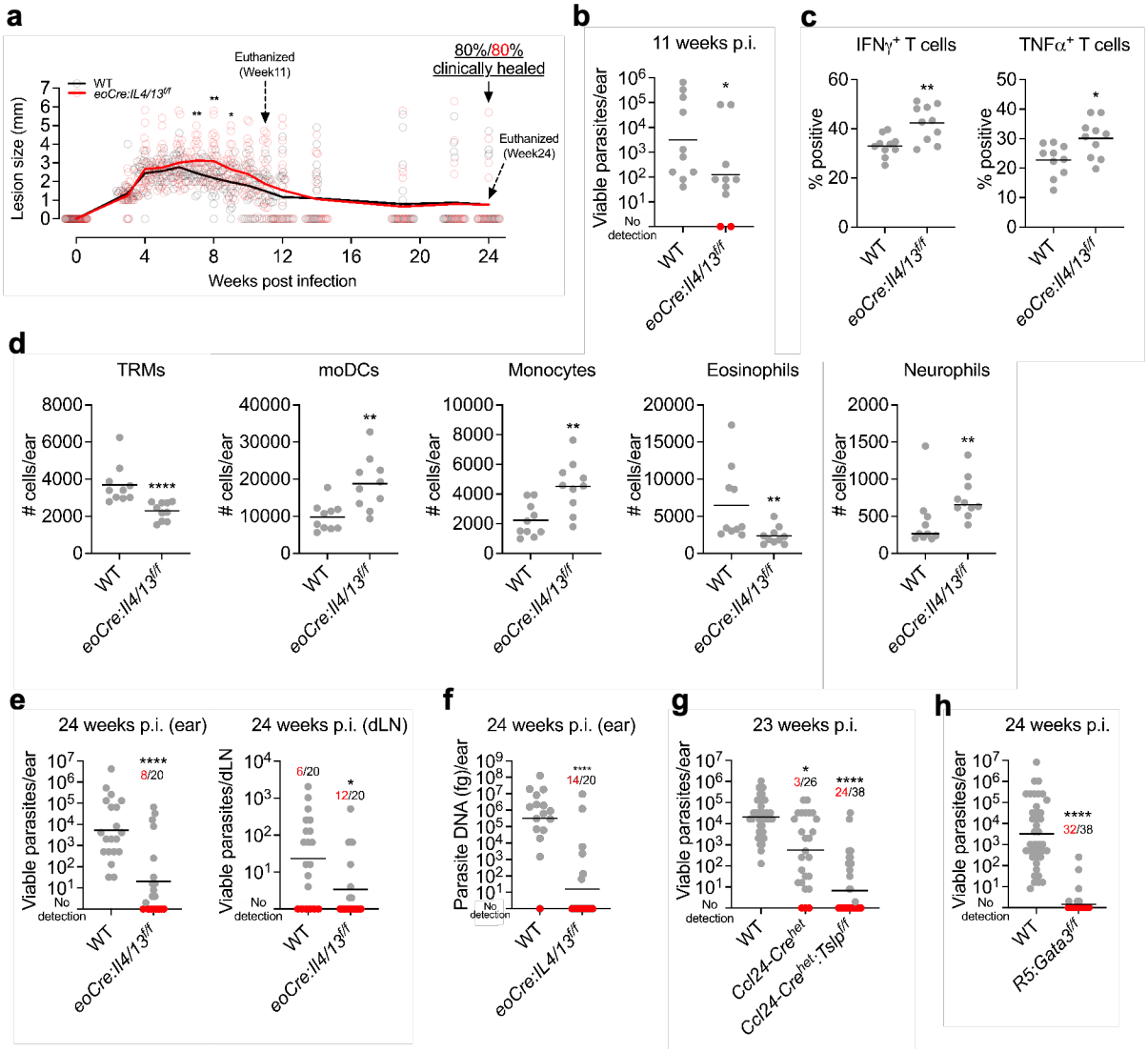


Figure 5. Conditional disruption of type 2 immune circuits reduces persistent *L. major* infection after clinical healing.

(A) Clinical course of infection in *eoCre:Il4/13*$^{f/f}$ and WT B/6 mice following intradermal inoculation with LmFn, showing lesion development and subsequent resolution. Each symbol represents an individual ear lesion measurement at the indicated time point; lines connect mean values. Mice were euthanized at 11 or 24 weeks post-infection for the analyses shown in subsequent panels. **(B)** Viable parasite burdens in one-tenth of ear homogenates from *eoCre:Il4/13*$^{f/f}$ and WT mice at 11 weeks post-infection, as determined by limiting dilution assay.

Red symbols indicate samples with no detectable parasite growth *ex vivo*. **(C)** Frequencies of IFNγ^+ and TNFα^+ T cells in the remaining nine-tenths of ear tissue from *eoCre:Il4/13*$^{f/f}$ and WT mice at 11 weeks post-infection, as determined by flow cytometry. **(D)** Numbers of the indicated immune cell populations in the same ear samples analyzed in (C). **(E)** Viable parasite burdens in whole ears and draining lymph nodes (dLNs) from *eoCre:Il4/13*$^{f/f}$ and WT mice at 24 weeks post-infection, as determined by limiting dilution assay. **(F)** Quantification of parasite DNA by real-time PCR in total DNA isolated from clinically healed ears of an independent cohort of *eoCre:Il4/13*$^{f/f}$ and WT mice at 24 weeks post-infection. **(G, H)** Viable parasite burdens in whole-ear homogenates from *Ccl24-Cre*^{het}*:Tslp*$^{f/f}$, Ccl24-Cre^{het}, *R5:Gata3*$^{f/f}$, and WT mice at 23–24 weeks post-infection, as determined by limiting dilution assay. In limiting dilution assays, red symbols indicate samples with no detectable parasite growth *ex vivo*; in (F), red symbols indicate samples with no detectable parasite DNA. Data are representative of at least two independent experiments. Individual values and geometric means are shown in (B) and (E–H); individual values and arithmetic means are shown in (C, D). *P* values were determined by non-parametric Mann-Whitney test; **P* < 0.05, ***P* < 0.01, ****P* < 0.001, *****P* < 0.0001.

Figure6

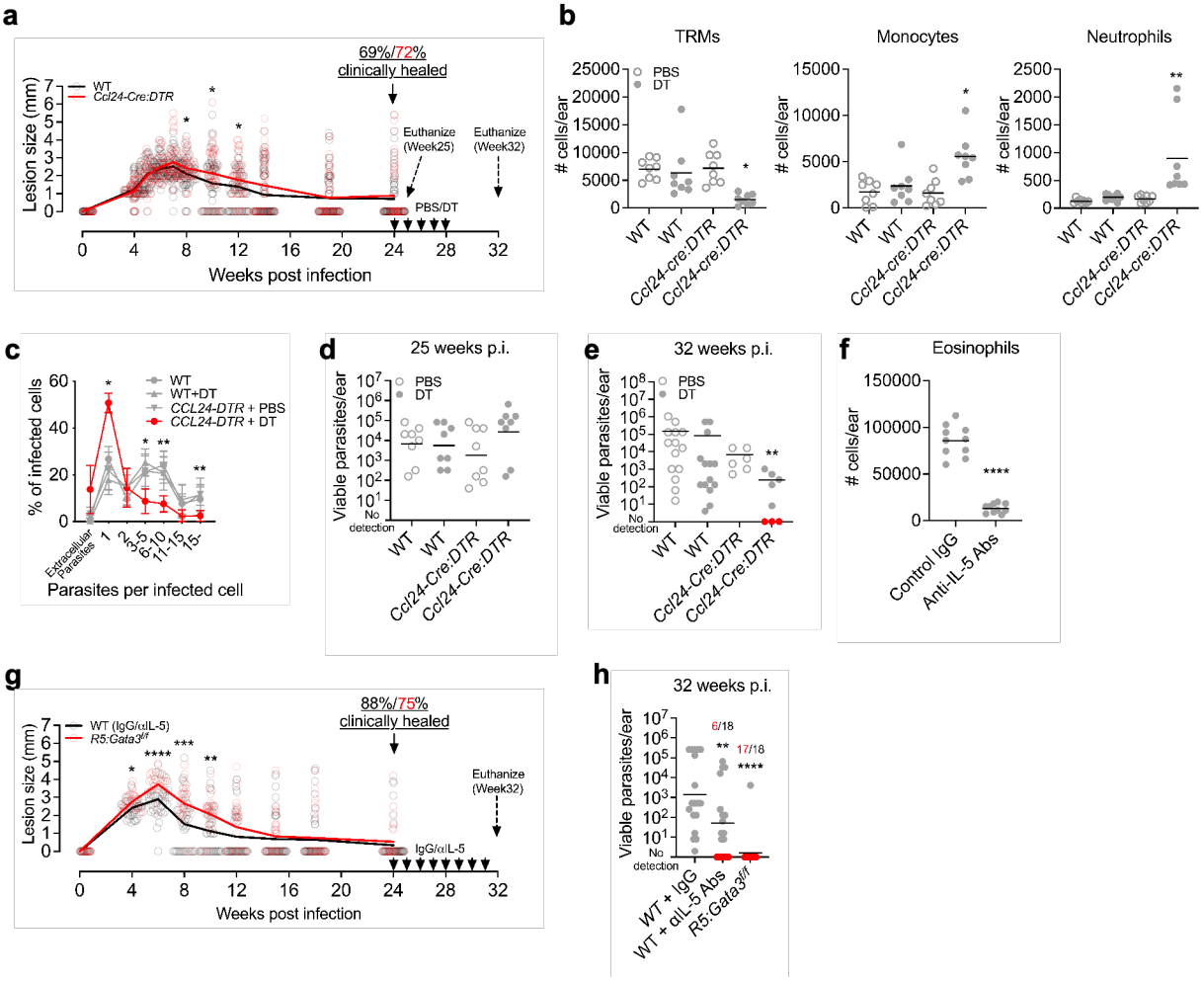
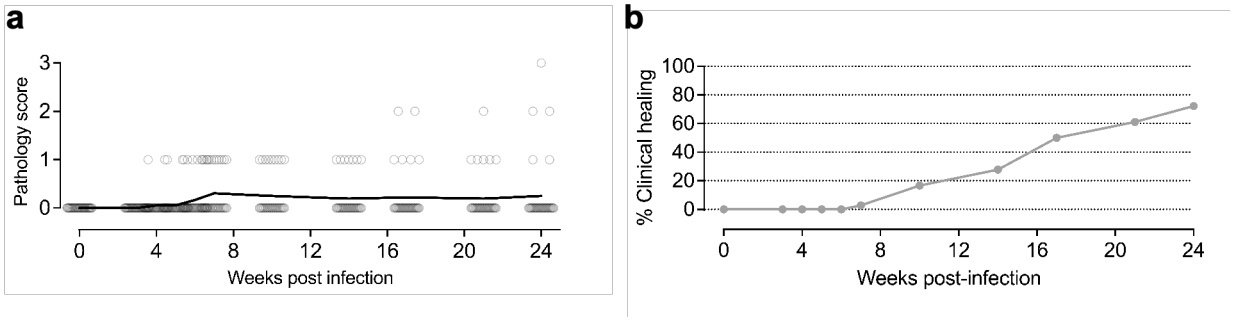


Figure 6. Targeted depletion of dermal TRMs and IL-5 neutralization reduce persistent *L. major* infection after clinical healing.

(A) Clinical course of infection in *Ccl24-Cre:DTR* and WT B/6 mice following intradermal LmFn infection, showing lesion development and subsequent resolution. Each symbol represents an individual ear lesion measurement at the indicated time point; lines connect mean values. Following clinical healing at 24 weeks post-infection, *Ccl24-Cre:DTR* and WT mice were treated with either PBS or diphtheria toxin (DT) once weekly, as indicated by arrowheads. **(B)** Flow cytometric quantification of the indicated cell populations in eight-tenths of ear tissue at 25 weeks post-infection, one week after the first administration of PBS or DT. **(C)** Cytospin analysis of one-tenth of ear tissue from the mice analyzed in (B). Infected cells were categorized

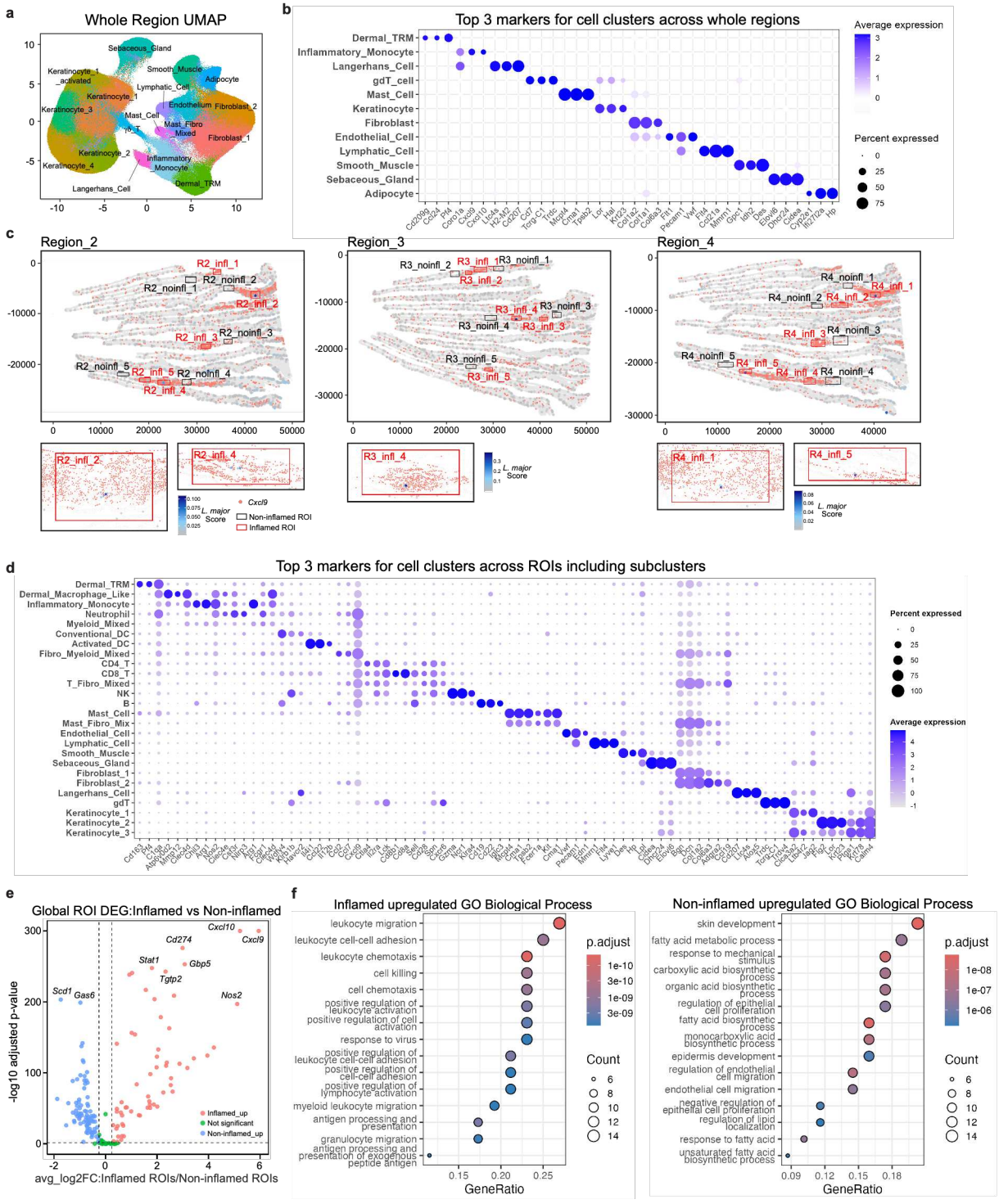
according to the number of intracellular parasites (1, 2, 3–5, 6–10, 11–15, or >15 parasites per infected cell), and extracellular parasites were quantified separately. **(D)** Viable parasite burdens in the remaining one-tenth of ear tissue from the mice analyzed in (B), as determined by limiting dilution assay. **(E)** Viable parasite burdens in whole-ear homogenates at 32 weeks post-infection following five repeated weekly administration of PBS or DT and a subsequent 4-week treatment-free period. **(F)** Flow cytometric quantification of eosinophils in ear tissue from WT mice following intradermal LmFn infection and intraperitoneal administration of control IgG or anti-IL-5 antibody on days 3 and 7 post-infection. **(G)** Clinical course of infection in WT B/6 and *R5:Gata3*$^{f/f}$ mice following intradermal LmFn infection. Each symbol represents an individual ear lesion measurement at the indicated time point; lines connect mean values. Following clinical healing at 24 weeks post-infection, WT mice were divided into two groups and treated with control IgG or anti-IL-5 antibody once weekly, as indicated by arrowheads. **(H)** Viable parasite burdens in whole-ear homogenates from the indicated groups at 32 weeks post-infection. Red symbols indicate samples with no detectable parasite growth *ex vivo*, and red fractions indicate the number of samples with no detectable parasites relative to the total number analyzed. Individual values and geometric means are shown in (D, E, H); individual values and arithmetic means are shown in (B, F). Data in (C) are shown as mean ± SD. *P* values were determined using non-parametric Mann-Whitney test; **P* < 0.05, ***P* < 0.01, ****P* < 0.001, *****P* < 0.0001.

Supplementary Figure1



Supplementary Figure 1. Clinical resolution of low-dose *L. major* infection in B/6 mice. **(A)** Pathology scores over the course of infection following intradermal inoculation of 1,000 *LmFn* metacyclic promastigotes into the ear dermis of B/6 mice. Pathology was scored as follows: 0, no visible lesion; 1, ulceration; 2, erosion of approximately half of the ear; and 3, complete erosion of the ear. Each symbol represents an individual ear, and the solid line indicates the mean pathology score at each time point. **(B)** Cumulative percentage of infected ears achieving clinical healing over the course of infection (n = 36 ears). Clinical healing was defined as the complete absence of visible skin pathology, including induration, erythema, and ulceration, at the site of parasite inoculation.

Supplementary Figure2

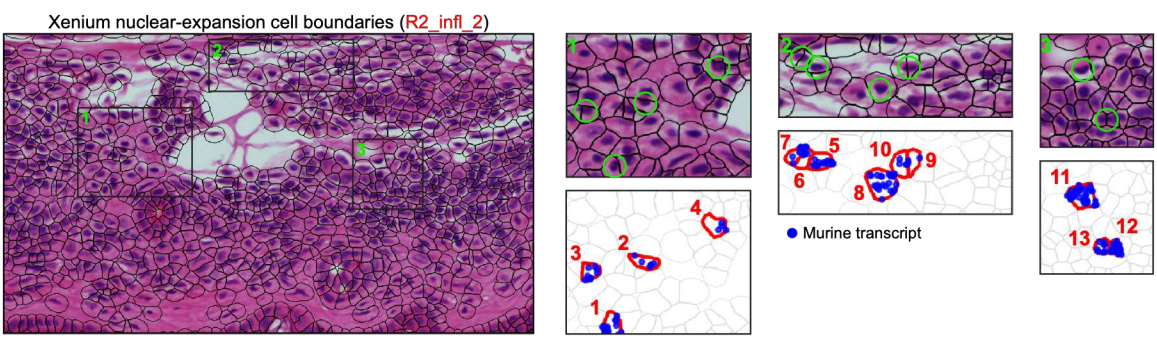


Supplementary Figure 2. Xenium spatial transcriptomic analysis of persistent infection sites in healed B/6 ears.

(A) UMAP visualization of all cells recovered from four Xenium tissue sections following StarDist-Baysor segmentation and unsupervised clustering. Major cell populations identified across the merged whole-region dataset are indicated. **(B)** Dot plot showing the top three marker genes used to define each major cell population identified in the whole-region dataset. **(C)** Spatial mapping of *Cxcl9* expression and *L. major* transcript scores in Regions 2 - 4 from healed B/6 ears at 24 weeks post-infection. ROIs exhibiting focal *Cxcl9* expression were designated as inflamed ROIs (red boxes), whereas adjacent regions with minimal *Cxcl9* expression were selected as matched non-inflamed ROIs (black boxes). Lower panels show selected inflamed ROIs containing focal *Cxcl9* expression and *L. major* transcript signals. **(D)** Dot plot showing the top three marker genes used to define cell populations identified in the merged ROI dataset following secondary clustering of inflamed and non-inflamed ROIs, including lymphocyte and myeloid subclusters. **(E)** Volcano plot showing differentially expressed genes (DEGs) between inflamed and non-inflamed ROIs. Genes enriched in inflamed ROIs are shown in red, genes enriched in non-inflamed ROIs are shown in blue, and non-significant genes are shown in green. **(F)** Gene Ontology (GO) Biological Process enrichment analysis of genes upregulated in inflamed and non-inflamed ROIs.

Supplementary Figure3

a



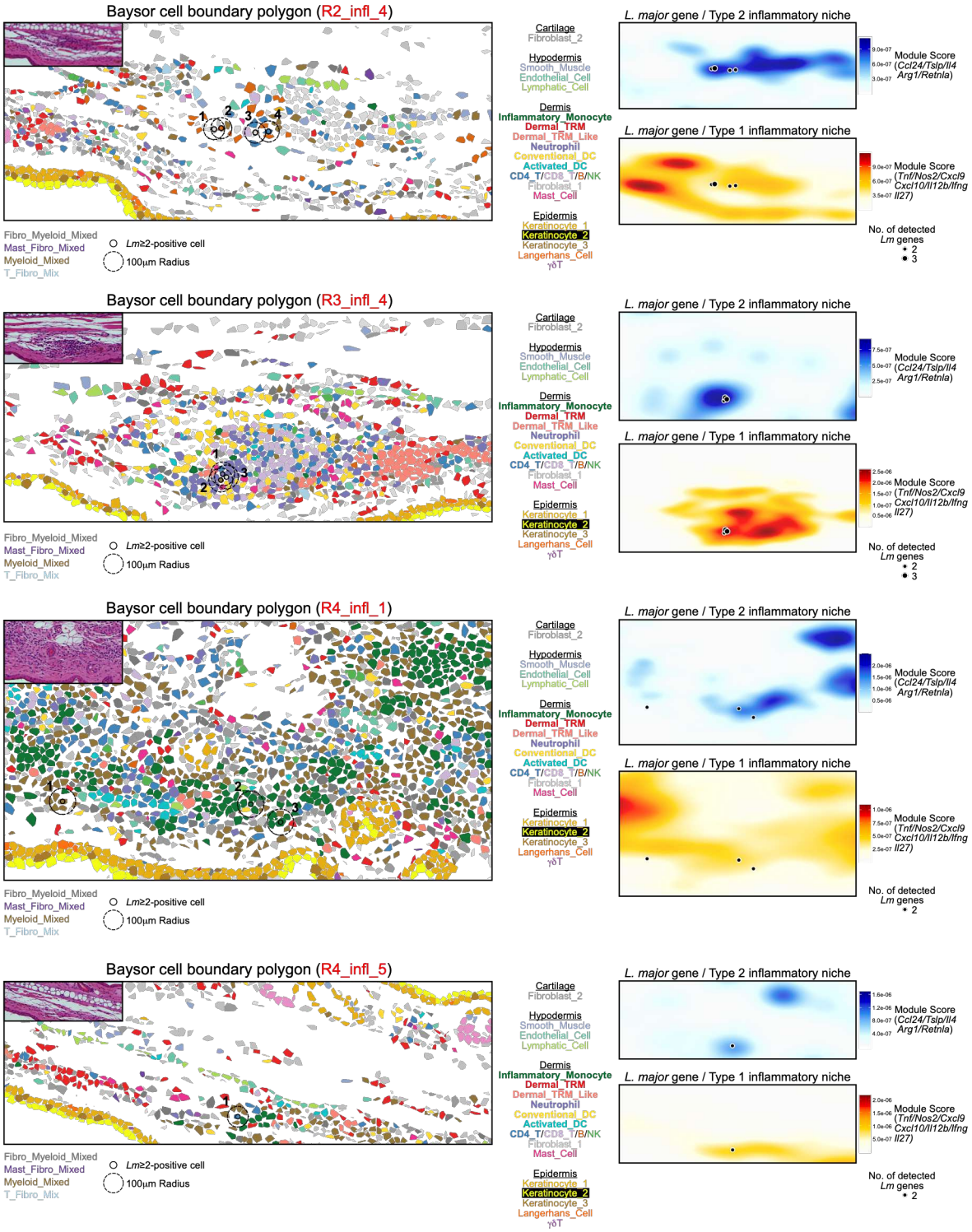
b

Cell_id	Xenium_cell_id	Total_transcripts	Detected_genes	Genes
1	ihhbmoho-1	23	19	AA467197, Adam8, C1qa, Ccl11 (2), Ccl25, Col1a2 (2), Col6a3, Cxcl9, Lgals1, Lgals3, Ly6c2 (2), Ly6e, Lyz1, Pgm2l1, Prdx6, Renbp, Sdha, Stat1, Vim (2)
2	ihgeicpf-1	6	5	Ccl19, Cxcl9 (2), Hdac9, Lgals3, Zyx
3	ihfplini-1	9	9	Ccl11, Cd40, Cxcl9, Fos, Il18bp, Mrc1, Pkm, Postn, Wfdc21
4	ihjbeklf-1	4	4	Arhgef37, Cxcl9, Klf4, S100a4
5	ihnoejka-1	15	14	Adgra2, Bgn, Ccl11, Cd2, Cmpk2, Col1a2, Col5a2, Col6a1, Cxcl9, Padi4, Prdx6, Ptges, Stat1 (2), Txnip
6	ihocnijb-1	6	6	Csf1r, Postn, Retnlg, Sell, Socs1, UnassignedCodeword_0043
7	ihodbbff-1	9	8	Ccl11 (2), Coro1a, Cxcl9, Dcn, Gas6, Il1r1, Itgam, Zyx
8	ihoeclco-1	26	16	Adgra2, Aldh1a2, Bgn, Ccl11 (4), Col1a2, Col6a1, Cxcl9 (2), H2-Eb1, Hif1a (2), Itgb2 (2), NegControlCodeword_0522, Tgfb1, Tgm2, Vim (4), Wdfy4, Zyx (2)
9	ihocbmpe-1	3	3	Arhgef37, Ccl8, Tgtp2
10	ihoahejm-1	5	5	Cxcl9, Il16, Itgam, Postn, Stat1
11	igfnoeof-1	35	22	AA467197 (2), Atp6v0d2, Bgn, Casp1, Clec4d (4), Col6a1, Ctsb, Cxcl9, Epcam, Fabp5 (2), Glipr2, Gpnmb (3), H3f3a, Hmox1, Il18bp, Lpl (2), Pkm (2), Postn, Sdc4, Spi1, Spn, Vim (5)
12	igfblpab-1	23	21	AA467197, Arg1, Bgn, Ccl11, Ccl24, Ccl7, Cxcl10, Cxcl9, H2-M2, Itgam, Ly6c2, Pdcd1lg2, Pgam1, Pkm (2), S100a4, Slc3a2, Tgm2, Tgtp2, Tnf, Txnip, Vim (2)
13	igfbaimj-1	8	7	Gpsm2, H2-Aa, Hexa, Lgals3, Ly6g, Pkm (2), Vim

Supplementary Figure 3. Histologically identified eosinophils exhibit low transcript recovery in Xenium spatial analysis.

(A) Representative H&E image of an inflamed Xenium region of interest (R2_inf_2) overlaid with cell boundaries generated by the Xenium nuclear-expansion segmentation algorithm. Three enlarged regions (right) highlight eosinophils identified histologically by their characteristic bilobed nuclei and eosinophilic cytoplasmic granules (green circles). Corresponding segmentation maps are shown below each inset. Blue dots indicate detected murine transcripts. Red outlines indicate Xenium segmentation objects spatially associated with histologically identified eosinophils, and red numbers identify the individual objects summarized in (B). **(B)** Transcriptomic features of the segmentation objects shown in (A). The table summarizes Xenium cell IDs, total transcript counts, numbers of detected genes, and representative expressed genes. Although eosinophils were readily identifiable by histology, the corresponding segmentation objects frequently contained few detected transcripts and lacked detectable expression of canonical eosinophil-associated genes included in the Xenium panel, limiting their transcriptomic identification.

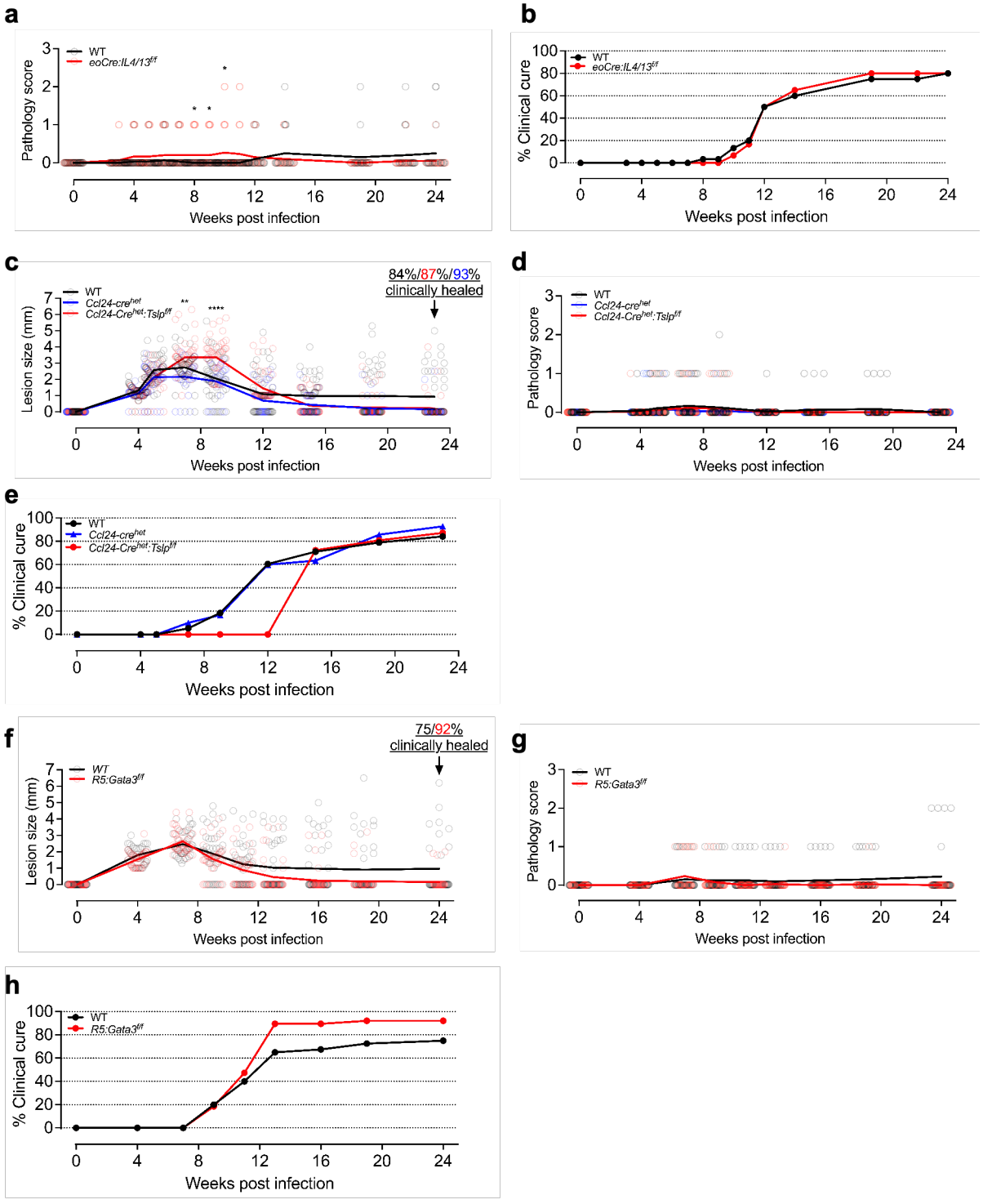
Supplementary Figure4



Supplementary Figure 4. Spatial organization of persistent parasite-associated foci in clinically healed skin.

Representative spatial maps of four inflamed Xenium regions of interest (R2_infl_4, R3_infl_4, R4_infl_1, and R4_infl_5) from clinically healed B/6 mice at 24 weeks post-infection. Left panels show Baysor-derived cell segmentation polygons colored according to cell identity alongside the corresponding H&E-stained Xenium sections. Cells assigned transcripts from two or more independently detected *L. major* genes (Lm≥2-positive cells) are indicated by open circles, and dashed circles denote the 100-μm-radius neighborhoods used for spatial neighborhood analysis. Right panels show the spatial distributions of Type 2 inflammatory niche scores (*Ccl24, Tslp, Il4, Arg1,* and *Retnla*) and Type 1 inflammatory niche scores (*Tnf, Nos2, Cxcl9, Cxcl10, Il12b, Ifng,* and *Il27*), with Lm≥2-positive cells overlaid.

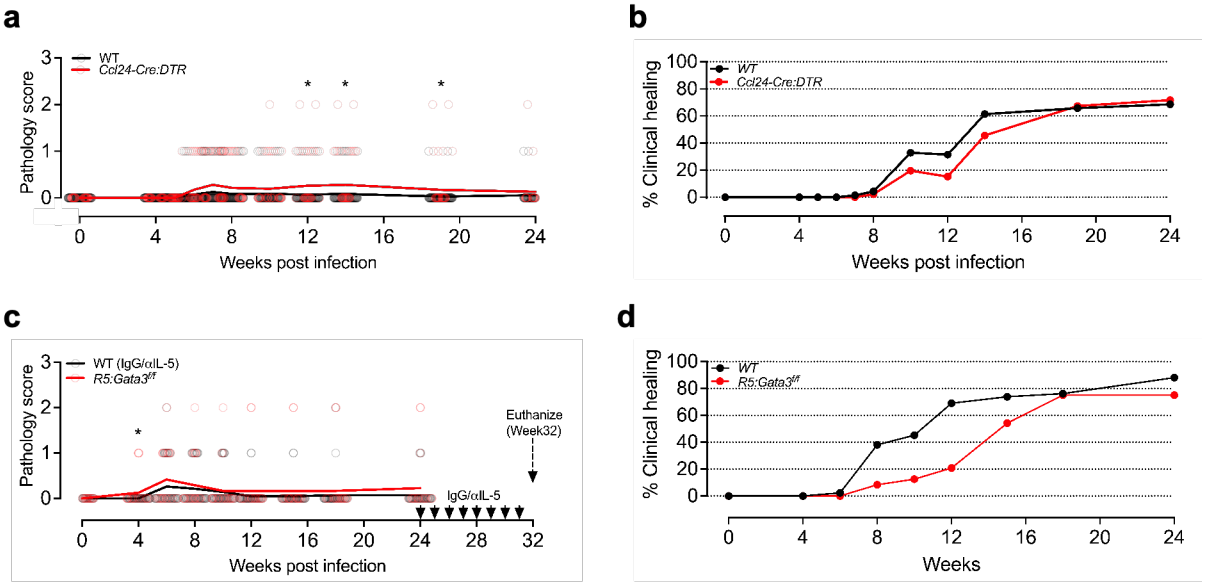
Supplementary Figure5



Supplementary Figure 5. Clinical disease progression and lesion resolution in genetically modified mouse strains.

(A, B) Pathology scores (A) and cumulative clinical healing rates (B) in WT and *eoCre:Il4/13*$^{f/f}$ mice following intradermal LmFn infection. **(C-E)** Lesion size (C), pathology scores (D), and cumulative clinical healing rates (E) in WT, *Ccl24-Cre*^{het}, and *Ccl24-Cre*^{het}*:Tslp*$^{f/f}$ mice following intradermal LmFn infection. **(F-H)** Lesion size (F), pathology scores (G), and cumulative clinical healing rates (H) in WT and *R5:Gata3*$^{f/f}$ mice following intradermal LmFn infection. Clinical healing was defined as the complete absence of visible skin induration and erythema at the inoculation site. Lesion size and pathology scores are shown as individual values with lines connecting mean values at each time point. *P* values were determined using non-parametric Mann-Whitney test; **P* < 0.05, ***P* < 0.01, ****P* < 0.001, *****P* < 0.0001.

Supplementary Figure6



Supplementary Figure 6. Clinical disease progression following dermal TRM depletion or IL-5 neutralization.

(A, B) Pathology scores (A) and cumulative clinical healing rates (B) in WT and *Ccl24-Cre:DTR* mice following intradermal LmFn infection. Mice were allowed to reach clinical healing before diphtheria toxin-mediated dermal TRM depletion. **(C, D)** Pathology scores (C) and cumulative clinical healing rates (D) in WT and *R5:Gata3$^{f/f}$* mice used in the IL-5 neutralization experiments. Following clinical healing at 24 weeks post-infection, WT mice were treated with control IgG or anti-IL-5 antibody as indicated in (C). Pathology scores are shown as individual values with lines connecting mean values at each time point. *P* values were determined using non-parametric Mann-Whitney test; *$P < 0.05$

1. Mendonca, M.G. *et al.* Persistence of leishmania parasites in scars after clinical cure of American cutaneous leishmaniasis: is there a sterile cure? *J Infect Dis* **189**, 1018–1023 (2004).

2. Ramirez, J.L. & Guevara, P. Persistent infections by Leishmania (Viannia) braziliensis. *Mem Inst Oswaldo Cruz* **92**, 333–338 (1997).

3. Schubach, A. *et al.* Cutaneous scars in American tegumentary leishmaniasis patients: a site of Leishmania (Viannia) braziliensis persistence and viability eleven years after antimonial therapy and clinical cure. *Am J Trop Med Hyg* **58**, 824–827 (1998).

4. Vergel, C. *et al.* Evidence for leishmania (viannia) parasites in the skin and blood of patients before and after treatment. *J Infect Dis* **194**, 503–511 (2006).

5. Choi, C.M. & Lerner, E.A. Leishmaniasis as an emerging infection. *J Investig Dermatol Symp Proc* **6**, 175–182 (2001).

6. Da-Cruz, A.M. *et al.* Atypical mucocutaneous leishmaniasis caused by Leishmania braziliensis in an acquired immunodeficiency syndrome patient: T-cell responses and remission of lesions associated with antigen immunotherapy. *Mem Inst Oswaldo Cruz* **94**, 537–542 (1999).

7. el Hassan, A.M. *et al.* Post kala-azar dermal leishmaniasis in the Sudan: clinical features, pathology and treatment. *Trans R Soc Trop Med Hyg* **86**, 245–248 (1992).

8. Saravia, N.G., Holguin, A.F., McMahon-Pratt, D. & D'Alessandro, A. Mucocutaneous leishmaniasis in Colombia: Leishmania braziliensis subspecies diversity. *Am J Trop Med Hyg* **34**, 714–720 (1985).

9. Vardy, D.A., Cohen, A., Kachko, L., Zvulunov, A. & Frankenburg, S. Relapse of cutaneous leishmaniasis in a patient with an infected subcutaneous rheumatoid nodule. *Br J Dermatol* **141**, 914–917 (1999).

10. Kimblin, N. *et al.* Quantification of the infectious dose of Leishmania major transmitted to the skin by single sand flies. *Proc Natl Acad Sci U S A* **105**, 10125–10130 (2008).

11. Svobodova, M. & Votypka, J. Experimental transmission of Leishmania tropica to hamsters and mice by the bite of Phlebotomus sergenti. *Microbes Infect* **5**, 471–474 (2003).

12. Laurenti, M.D. *et al*. Asymptomatic dogs are highly competent to transmit Leishmania (Leishmania) infantum chagasi to the natural vector. *Vet Parasitol* **196**, 296–300 (2013).

13. Aebischer, T., Moody, S.F. & Handman, E. Persistence of virulent Leishmania major in murine cutaneous leishmaniasis: a possible hazard for the host. *Infect Immun* **61**, 220–226 (1993).

14. Nicolas, L., Sidjanski, S., Colle, J.H. & Milon, G. Leishmania major reaches distant cutaneous sites where it persists transiently while persisting durably in the primary dermal site and its draining lymph node: a study with laboratory mice. *Infect Immun* **68**, 6561–6566 (2000).

15. Belkaid, Y. *et al*. The role of interleukin (IL)-10 in the persistence of Leishmania major in the skin after healing and the therapeutic potential of anti-IL-10 receptor antibody for sterile cure. *J Exp Med* **194**, 1497–1506 (2001).

16. Stenger, S., Donhauser, N., Thuring, H., Rollinghoff, M. & Bogdan, C. Reactivation of latent leishmaniasis by inhibition of inducible nitric oxide synthase. *J Exp Med* **183**, 1501–1514 (1996).

17. Stobie, L. *et al*. The role of antigen and IL-12 in sustaining Th1 memory cells in vivo: IL-12 is required to maintain memory/effector Th1 cells sufficient to mediate protection to an infectious parasite challenge. *Proc Natl Acad Sci U S A* **97**, 8427–8432 (2000).

18. Sacks, D.L. Vaccines against tropical parasitic diseases: a persisting answer to a persisting problem. *Nat Immunol* **15**, 403–405 (2014).

19. Bogdan, C. *et al*. Fibroblasts as host cells in latent leishmaniosis. *J Exp Med* **191**, 2121–2130 (2000).

20. Schwing, A. *et al*. Identification of adipocytes as target cells for Leishmania infantum parasites. *Sci Rep* **11**, 21275 (2021).

21. Valigurova, A. & Kolarova, I. Unrevealing the Mystery of Latent Leishmaniasis: What Cells Can Host Leishmania? *Pathogens* **12** (2023).

22. Lee, S.H. *et al*. Mannose receptor high, M2 dermal macrophages mediate nonhealing Leishmania major infection in a Th1 immune environment. *J Exp Med* **215**, 357–375 (2018).

23. Lee, S.H. *et al.* M2-like, dermal macrophages are maintained via IL-4/CCL24-mediated cooperative interaction with eosinophils in cutaneous leishmaniasis. *Sci Immunol* **5** (2020).

24. Lee, S.H. *et al.* Dermis resident macrophages orchestrate localized ILC2 eosinophil circuitries to promote non-healing cutaneous leishmaniasis. *Nat Commun* **14**, 7852 (2023).

25. Yamazaki, T. *et al.* Whole-Mount Adult Ear Skin Imaging Reveals Defective Neuro-Vascular Branching Morphogenesis in Obese and Type 2 Diabetic Mouse Models. *Sci Rep* **8**, 430 (2018).

26. Radtke, A.J. *et al.* IBEX: an iterative immunolabeling and chemical bleaching method for high-content imaging of diverse tissues. *Nat Protoc* **17**, 378–401 (2022).

27. Janesick, A. *et al.* High resolution mapping of the tumor microenvironment using integrated single-cell, spatial and in situ analysis. *Nat Commun* **14**, 8353 (2023).

28. Barreiro, O. *et al.* Pivotal role for skin transendothelial radio-resistant anti-inflammatory macrophages in tissue repair. *Elife* **5** (2016).

29. Sheng, J., Ruedl, C. & Karjalainen, K. Most Tissue-Resident Macrophages Except Microglia Are Derived from Fetal Hematopoietic Stem Cells. *Immunity* **43**, 382–393 (2015).

30. Baranska, A. *et al.* Unveiling skin macrophage dynamics explains both tattoo persistence and strenuous removal. *J Exp Med* **215**, 1115–1133 (2018).

31. Mandell, M.A. & Beverley, S.M. Continual renewal and replication of persistent Leishmania major parasites in concomitantly immune hosts. *Proc Natl Acad Sci U S A* **114**, E801–E810 (2017).

32. Voisin, B. *et al.* Macrophage-mediated extracellular matrix remodeling controls host Staphylococcus aureus susceptibility in the skin. *Immunity* **56**, 1561–1577 e1569 (2023).

33. Keating, G.M. Mepolizumab: First Global Approval. *Drugs* **75**, 2163–2169 (2015).

34. Markham, A. Reslizumab: First Global Approval. *Drugs* **76**, 907–911 (2016).

35. Markham, A. Benralizumab: First Global Approval. *Drugs* **78**, 505–511 (2018).

36. Spath, G.F. & Beverley, S.M. A lipophosphoglycan-independent method for isolation of infective Leishmania metacyclic promastigotes by density gradient centrifugation. *Exp Parasitol* **99**, 97–103 (2001).

37. Belkaid, Y. *et al*. A natural model of Leishmania major infection reveals a prolonged "silent" phase of parasite amplification in the skin before the onset of lesion formation and immunity. *J Immunol* **165**, 969–977 (2000).

38. Belkaid, Y. *et al*. Development of a natural model of cutaneous leishmaniasis: powerful effects of vector saliva and saliva preexposure on the long-term outcome of Leishmania major infection in the mouse ear dermis. *J Exp Med* **188**, 1941–1953 (1998).

39. Antonia, A.L., Wang, L. & Ko, D.C. A real-time PCR assay for quantification of parasite burden in murine models of leishmaniasis. *PeerJ* **6**, e5905 (2018).

40. Guizar-Sicairos, M., Thurman, S.T. & Fienup, J.R. Efficient subpixel image registration algorithms. *Opt Lett* **33**, 156–158 (2008).